# Ionic and electronic properties of the topological insulator $Bi_2Te_2Se$ investigated via $\beta$-detected nuclear magnetic relaxation and resonance of $^8$Li

Ryan M. L. McFadden,[1,2,*] Aris Chatzichristos,[2,3] Kim H. Chow,[4] David L. Cortie,[1,2,3,†] Martin H. Dehn,[2,3] Derek Fujimoto,[2,3] Masrur D. Hossain,[3,‡] Huiwen Ji,[5,§] Victoria L. Karner,[1,2] Robert F. Kiefl,[2,3,6] C. D. Philip Levy,[6] Ruohong Li,[6] Iain McKenzie,[6,7] Gerald D. Morris,[6] Oren Ofer,[6] Matthew R. Pearson,[6] Monika Stachura,[6] Robert J. Cava,[5] and W. Andrew MacFarlane[1,2,6,‖]

[1]*Department of Chemistry, University of British Columbia, Vancouver, BC, Canada V6T 1Z4*
[2]*Stewart Blusson Quantum Matter Institute, University of British Columbia, Vancouver, BC, Canada V6T 1Z4*
[3]*Department of Physics and Astronomy, University of British Columbia, Vancouver, BC, Canada V6T 1Z1*
[4]*Department of Physics, University of Alberta, Edmonton, AB, Canada T6G 2E1*
[5]*Department of Chemistry, Princeton University, Princeton, New Jersey 08544, USA*
[6]*TRIUMF, 4004 Wesbrook Mall, Vancouver, BC, Canada V6T 2A3*
[7]*Department of Chemistry, Simon Fraser University, Burnaby, BC, Canada V5A 1S6*

(Received 26 October 2018; revised manuscript received 15 February 2019; published 8 March 2019)

We report measurements on the high-temperature ionic and low-temperature electronic properties of the three-dimensional topological insulator $Bi_2Te_2Se$ using ion-implanted $^8$Li $\beta$-detected nuclear magnetic relaxation and resonance. With implantation energies in the range 5–28 keV, the probes penetrate beyond the expected range of the topological surface state, but are still within 250 nm of the surface. At temperatures above ∼150 K, spin-lattice relaxation measurements reveal isolated $^8Li^+$ diffusion with an activation energy $E_A = 0.185(8)$ eV and attempt frequency $\tau_0^{-1} = 8 \pm 3 \times 10^{11} s^{-1}$ for atomic site-to-site hopping. At lower temperature, we find a linear Korringa-type relaxation mechanism with a field-dependent slope and intercept, which is accompanied by an anomalous field dependence to the resonance shift. We suggest that these may be related to a strong contribution from orbital currents or the magnetic freeze-out of charge carriers in this heavily compensated semiconductor, but that conventional theories are unable to account for the extent of the field dependence. Conventional NMR of the stable host nuclei may help elucidate their origin.

DOI: 10.1103/PhysRevB.99.125201

## I. INTRODUCTION

Bismuth chalcogenides with the formula $Bi_2Ch_3$ (Ch = S, Se, Te) are narrow-gap semiconductors that have been studied for decades for their thermoelectric properties. They crystallize in the layered tetradymite structure [1,2], consisting of stacks of strongly bound Ch-Bi-Ch-Bi-Ch quintuple layers (QLs) loosely coupled by van der Waals (vdW) interactions (see Fig. 1). More recently, interest in their electronic properties has exploded [3] following the realization that strong spin-orbit coupling and band inversion combine to make them three-dimensional (3D) topological insulators (TIs) [4], characterized by a gapless topological surface state (TSS). Electronically, this family of TIs is characterized by a relatively insulating bulk and a robustly conductive surface, with greater contrast in conductivity between the two regions significantly facilitating identification and study. The prevalence for self-doping in binary chalcogenides (e.g., $Bi_2Se_3$ or $Bi_2Te_3$) often yields crystals far from insulating in the bulk, masking the signature of the conductive surface state. This has been mitigated, for example, in the most widely studied tetradymite TI $Bi_2Se_3$ with Ca doping to suppress the more usual *n*-type conductivity [5,6]. On the other hand, the stoichiometric ordered [7,8] ternary line compound $Bi_2Te_2Se$ (BTS) exhibits a much lower conductivity thanks to its fortuitous crystal chemistry [8], with antisite defects (e.g., bismuth substitution on a tellurium site) playing an important role [9]. Indeed, BTS crystals with a characteristic bulk band gap of ∼0.3 eV [10] have demonstrated such desired large bulk resistivities at low temperatures [8,11–13]. A great deal is known about its surface properties, with angle-resolved photoemission spectroscopy (ARPES) revealing the characteristic linear dispersion about the Dirac point [9,14–19]; however, the material is not an ideal TI due to the close proximity of the Dirac point to the top of the bulk valence band [2].

With the novel electronic structure of the Bi chalcogenides evident primarily in the TSS, much inquiry has focused on surface-sensitive probes, such as ARPES, scanning tunneling spectroscopy (STS), and transport. On the other hand, NMR is well known to reveal electronic properties in metals through hyperfine coupling of the nucleus to surrounding electron

*rmlm@chem.ubc.ca
†Current address: Institute for Superconducting and Electronic Materials, Australian Institute for Innovative Materials, University of Wollongong, North Wollongong, NSW 2500, Australia.
‡Current address: ASML US, Inc, 399 W Trimble Rd, San Jose, CA 95131, USA.
§Current address: Department of Materials Science and Engineering, University of California, Berkeley, Berkeley, CA 94720, USA.
‖wam@chem.ubc.ca

 

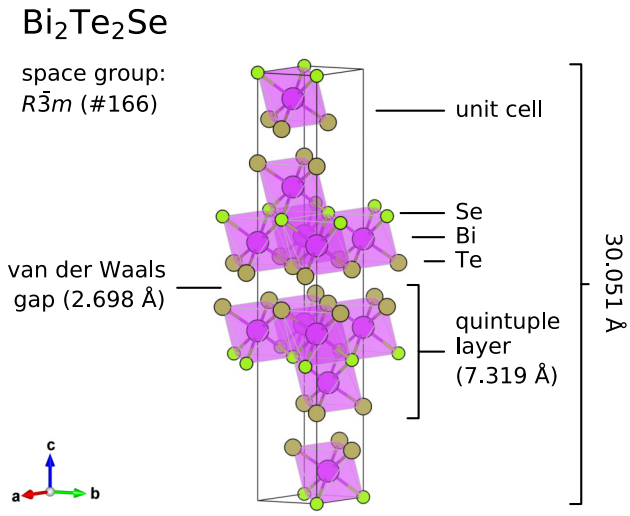


FIG. 1. Crystal structure of $Bi_2Te_2Se$ [8], consisting of Te-Bi-Se-Bi-Te layers. These quintuple layers are weakly coupled through van der Waals interactions, giving rise to a characteristic gap between adjacent Te planes. This atomic arrangement is analogous to transition metal dichalcogenides, where it is possible to insert foreign atoms and small molecules within the van der Waals gap. The structure was drawn using VESTA [20].

spins that gives rise to the Knight shift, a measure of the Pauli spin susceptibility, and the Korringa spin-lattice relaxation (SLR) [21,22]. Theory predicts dramatic effects in such quantities for the TSS [23], but NMR is generally a bulk probe with very little sensitivity to the surface. Despite this, a considerable body of conventional NMR in the $Bi_2Ch_3$ TIs has accumulated. Since these results are closely related to this study, we give a brief summary.

All elements in BTS have NMR-active isotopes. The most conspicuous feature of 100% abundant $^{209}$Bi NMR is the strong quadrupolar interaction. However, the broad quadrupole pattern shows clear evidence of a shift related to carrier density, indicating a very strong hyperfine coupling [24], confirmed more recently by very high-field NMR [25]. The behavior of $1/T_1$ is less consistent, with results ranging from $T$ linear to nearly $T$ independent [24,26] at low temperature. The low abundance (∼7%) pure magnetic spin-$\frac{1}{2}$ probes $^{77}$Se and $^{125}$Te show a small $T$-independent shift, and Korringa relaxation at low temperature in orientationally averaged powder spectra [27]. This Korringa relaxation is enhanced in nanocrystals and was attributed to the TSS [28], but given the evidence for aging effects that stabilize a conventional metallic surface state [29], this connection remains unclear. More recent work in single crystals has identified distinct resonances from inequivalent chalcogen planes, and a more detailed analysis of the chalcogen NMR is required [30–32].

While a great deal is known about the TSS from surface-sensitive probes, little is known about how this behavior transitions to the bulk as a function of depth below the crystal surface. We plan to address this question using highly spin-polarized radioactive ions, specifically, using depth-resolved $\beta$-detected nuclear magnetic resonance and relaxation ($\beta$-NMR) [33] with short-lived $^8$Li as the probe nucleus, similar to low-energy muon spin rotation ($\mu$SR) [34]. As a first step, here we present results using relatively high implantation energies, 5–28 keV, corresponding to $^8Li^+$ implantation depths below the TSS. We find that below ∼150 K $^8$Li experiences strongly field-dependent relaxation and resonance shifts. The relaxation is $T$ linear and reminiscent of a Korringa mechanism, but conventional theory for NMR cannot account for its field dependence, which we suggest is due to magnetic carrier freeze-out. At higher temperatures, an additional relaxation mechanism is observed, originating from ionic diffusion of isolated $^8Li^+$ in the vdW gap.

The remainder of the paper is organized as follows: A brief description of the experiment is given in Sec. II, followed by the results and analysis in Sec. III. A detailed discussion is given in Sec. IV, focusing on the high-temperature dynamics of the isolated $^8Li^+$ ion in the vdW gap (Sec. IV A), and the electronic properties of BTS giving rise to the field-dependent relaxation and resonance shifts at low temperature (Sec. IV B). Finally, a concluding summary can be found in Sec. V.

## II. EXPERIMENT

Since implanted ion $\beta$-NMR is not a widely known technique, here we summarize some of its main features. More detailed accounts can be found in Refs. [33,35].

### A. $\beta$-NMR technique

In many ways, $\beta$-NMR is very similar to stable isotope NMR [22]. The nuclear spin senses the local magnetic fields via the Zeeman interaction and their time averages contribute to the resonance shift and line shape. In addition, since $^8$Li possesses a nonzero nuclear quadrupole moment, the nuclear spin is coupled to the local electric field gradient (EFG) [22,36]

$$eq = \frac{\partial^2 V}{\partial x_i \partial x_j},$$

a tensor that is zero under cubic symmetry. When the EFG tensor is nonvanishing, the quadrupolar interaction splits the resonance into a set of $2I$ satellites. The integer spin ($I = 2$) of $^8$Li (uncommon in conventional NMR) has the important consequence that the quadrupolar spectrum has no "main line" at the Larmor frequency,

$$\omega_0 = 2\pi\nu_0 = \gamma B_0,$$

determined by the gyromagnetic ratio $\gamma$ of the NMR nucleus and the (dominant) applied magnetic field $B_0$. In contrast, for the more familiar case of half-integer $I$, the $m = \pm\frac{1}{2}$ transition yields, to first order, a line at $\nu_0$ unperturbed by quadrupole effects [36]. While the quadrupole interaction is often the most important perturbation to the nuclear spin energy levels in nonmagnetic materials, for $^8$Li it is still relatively small (in the kHz range), because its nuclear electric quadrupole moment $Q$ is small, compared, for example, to $^{209}$Bi.

Distinct from conventional NMR, the probe is extrinsic to the host, and its lattice site is not known *a priori*. Like the implanted positive muon $\mu^+$ in $\mu$SR, the $^8Li^+$ ion generally stops in a high-symmetry site in a crystalline host. Some site

information is available in the resonance spectrum since the local field and EFG depend on the site, but generally one has to combine this information with knowledge of the structure and calculations to make a precise site assignment. Moreover, $^8Li^+$, as a light interstitial, can often be *mobile* near room temperature. In this case, the local interactions become time dependent, as the probe undergoes stochastic hopping, usually among interstitial sites. If the average hop rate is near the Larmor frequency, this will cause SLR [37–39]. Since this process is independent of other relaxation mechanisms due to the intrinsic fluctuations of the host, the rates simply add. At accessible beam intensities, the instantaneous number of $^8$Li in the sample never exceeds $\sim 10^6$, meaning $^8$Li is always present in the ultradilute limit, and interactions between $^8$Li can be neglected. Any diffusive motion is thus characteristic of the *isolated* interstitial.

As with conventional NMR, the SLR is determined by fluctuations at the Larmor frequency in the radio-frequency (RF) range. Specific to the $\beta$-NMR mode of detection, the range of measurable $T_1$ relaxation times is determined by the radioactive lifetime $\tau_\beta$. As a rule of thumb, measurable $T_1$ values lie in the range $0.01\tau_\beta$ to $100\tau_\beta$ [35]. Near the upper end of this range, the spin relaxation is very slow and exhibits little or no curvature on the timescale of the measurement. One can still measure the relaxation rate from the slope, but it is significantly correlated to the initial amplitude of the relaxing polarization signal.

In conventional NMR, the signal-to-noise ratio is proportional to the square of the Larmor frequency, favoring high applied fields. Consequently, for practical reasons, NMR is often done at a single fixed field in the range of $\sim$10 T. In contrast, the signal in $\beta$-NMR is independent of frequency, and the field can easily be varied. This can be useful, for example, in identifying relaxation mechanisms with distinct field dependencies. In addition, this enables $\beta$-NMR in the realm of low applied fields (up to tens of mT). As the applied field approaches zero, fluctuations of the stable magnetic *nuclei* of the host often become the dominant source of relaxation. At such low fields, distinction of different nuclei by their Larmor frequency is suppressed, and the isolated $^8$Li begins to resonantly lose its spin polarization to the bath of surrounding nuclear spins. Effectively, this simply appears as another relaxation mechanism active only at low fields. The extent of the low-field regime depends on the moment, density, and NMR properties of the host lattice nuclei.

In many aspects, $\beta$-NMR is also quite similar to $\mu$SR [34], which too relies on the anisotropic $\beta$ decay from the implanted $\mu^+$ to study internal fields in materials. The two techniques, however, have several important differences, largely due to the properties of their respective probes. In contrast to $^8$Li, $\mu^+$ is (1) a pure magnetic spin-$\frac{1}{2}$ probe with no quadrupolar interaction; (2) much shorter lived (lifetime $\sim$2.2 $\mu$s), making it sensitive to much faster SLR rates; and (3) chemically unlike an alkali cation, but rather analogous to isolated hydrogen, the basis for much of its use in semiconductors and semimetals [40]. Consequently, in TIs, $\mu$SR has mainly been used to study magnetically doped [41,42] or superconducting [43,44] compositions. In contrast, the $^8$Li relaxation rates we find here are too slow for $\mu$SR, and are in the range of conventional NMR.

### B. Measurements

A single crystal of BTS was grown as detailed in Ref. [8] and taken from the more insulating section of a larger boule. The insulating character was confirmed by resistivity measurements, which show an increase by a factor of $\sim$3 below 100K, with a low-temperature maximum $\sim$0.1 $\Omega$ cm, characteristic of the more insulating BTS compositions [8]. Prior to the $\beta$-NMR experiments, the crystal, with dimensions $5 \times 4 \times 0.1$ mm$^3$, was cleaved in air and affixed to a sapphire plate using Ag paint (SPI Supplies, West Chester, PA) for mounting on a cold finger cryostat.

$\beta$-NMR experiments were performed at TRIUMF's ISAC facility in Vancouver, Canada. A low-energy highly polarized beam of $^8Li^+$ was implanted into the BTS single crystal within one of two dedicated spectrometers [33,45–47]. The incident $^8Li^+$ ion beam had a typical flux of $\sim 10^6$ ions/s over a beam spot $\sim$2 mm in diameter. At the implantation energies $E$ used here (5–28 keV), the ions stop at average depths >30 nm (see Fig. 10 in Appendix A).

The probe nucleus $^8$Li has nuclear spin $I = 2$, gyromagnetic ratio $\gamma/2\pi = 6.3016$ MHz T$^{-1}$, nuclear electric quadrupole moment $Q = +32.6$ mb, and radioactive lifetime $\tau_\beta = 1.21$s. Spin polarization was achieved in flight by collinear optical pumping with circularly polarized light, yielding a polarization of $\sim$70% [48], and monitored after ion implantation through the anisotropic $\beta$-decay emissions of $^8$Li. Specifically, the experimental $\beta$-decay asymmetry (proportional to the average longitudinal spin polarization) was measured by combining the rates in two opposed scintillation counters [33,35]. The proportionality constant depends on the experimental geometry and the details of the $\beta$ decay, and is $\sim$0.1.

SLR measurements were performed by monitoring the transient decay of spin polarization both during and following a 4-s pulse of beam [49,50]. During the pulse, the polarization approaches a steady-state value, while after the pulse, it relaxes to $\sim$0. Note that the discontinuity at $t = 4$s (see Fig. 2) is characteristic of $\beta$-NMR SLR data. Unlike conventional NMR, no RF field is required for the SLR measurements, as the probe spins are implanted in a spin state already far from equilibrium. As a result, it is generally faster and easier to measure SLR than the resonance; however, as a corollary, this type of relaxation measurement has no spectral resolution and represents the spin relaxation of *all* the $^8$Li. Here, SLR rates were measured in small temperature steps from 3–317 K under applied magnetic fields between 2.20–6.55 T parallel to the trigonal $c$ axis, and with coarser temperature steps at lower magnetic fields (2.5–20 mT) perpendicular to the $c$ axis. A typical SLR measurement took $\sim$20 min.

Resonances were acquired in a continuous $^8Li^+$ beam with a continuous wave (CW) transverse RF magnetic field stepped slowly through the $^8$Li Larmor frequency. In this measurement mode, the spin of any on-resonance $^8$Li is rapidly precessed by the RF field, resulting in a loss in the average time-integrated asymmetry. The evolution of the resonance was recorded over a temperature range of 3 to 317 K in a dedicated high-field spectrometer [45,47] with a highly homogeneous magnetic field in the range of 2.20–6.55 T parallel to the BTS $c$ axis. The resonance frequency was calibrated against the position

in single crystal MgO (100) at 300 K [51], with the superconducting solenoid persistent. Resonance measurements typically took ∼30 min to acquire.

With this mode of measurement, the resonance amplitudes are determined by several factors, some quite distinct from conventional pulsed RF NMR. First, the maximum amplitude is determined by the baseline asymmetry [52], which represents a time integral of the SLR. It also depends on the magnitude of the RF magnetic field $B_1$ relative to the linewidth since the RF will only precess $^8$Li within a frequency window of width $\sim\gamma B_1$. The resonance amplitude may also be enhanced by slow spectral dynamics occurring up to the second timescale since the RF is applied at a particular frequency for an integration time of typically 1 s, and any $^8$Li that are resonant during this time will be precessed by it. Quadrupole satellite amplitudes are further reduced by the simple fact that saturating a single quantum transition ($\Delta m = \pm 1$) can, at most, reduce the asymmetry by 25% [48]. Unsplit resonances can, in contrast, be much larger, since all the $\Delta m = \pm 1$ transitions are resonant at the same frequency and, if saturated, the RF will precess the full polarization giving the full amplitude equal to the off-resonance asymmetry.

## III. RESULTS AND ANALYSIS

### A. Spin-lattice relaxation

Typical $^8$Li SLR data at high and low magnetic field in BTS are shown in Fig. 2 for several temperatures, where the spectra have been normalized by their $t = 0$ asymmetry ($A_0$). It is immediately evident that the SLR rates are strongly dependent on both temperature and field. In high fields, the relaxation is relatively slow, but comparable to that observed in some elemental metals [33] and semimetals [53]. Surprisingly, the relaxation is *faster* than in the normal state of the structurally similar $NbSe_2$ [54], despite a much smaller carrier density. However, it is also slower than in the 3D TI $Bi_{1-x}Sb_x$ [53]. At all temperatures, the relaxation rate increases monotonically with decreasing magnetic field. Even at very low temperatures near ∼10 K, where most excitations are frozen out, the SLR remains substantial. The relaxation rate at low field is orders of magnitude faster than in Tesla fields, suggesting the importance of low-field relaxation from the host lattice nuclear moments [55,56]. On top of the field dependence, there is also a strong temperature dependence; the relaxation rate increases with increasing $T$, but this trend is nonmonotonic and at least one temperature exists (per field) where the rate is *maximized*.

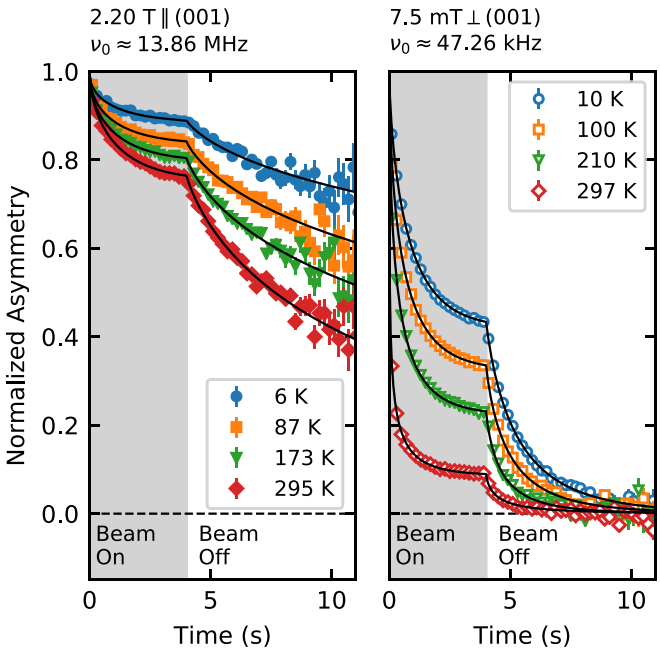


FIG. 2. $^8$Li spin-lattice relaxation data in $Bi_2Te_2Se$ at high and low magnetic fields. The characteristic kink at $t = 4$s corresponds to the trailing edge of the $^8Li^+$ beam pulse. The $^8$Li relaxation is strongly field dependent, increasing with decreasing magnetic field, and increases nonmonotonically with increasing temperature. The solid black lines are the result of a global fit to all spectra at a given field to a stretched exponential relaxation function, Eq. (1), convoluted with the square beam pulse [49,50].

We now consider a detailed analysis to quantify these observations. First, we remark that the relaxation is nonexponential at *all* temperatures and fields. The precise origin for this remains unclear. While it is well known that magnetic relaxation of quadrupolar spins is multiexponential, this is not the case here, as the initial polarization following optical pumping is purely dipolar, yielding single exponential magnetic relaxation, similar to the conventional NMR case where all the quadrupole satellites are simultaneously saturated [57]. If, however, the relaxation is quadrupolar (due to a fluctuating EFG), then in the slow limit for $I = 2$, the relaxation is biexponential [58]. In light of this, we use a phenomenological stretched exponential, consistent with the approach adopted in conventional NMR in similar materials [24,27,28,59]. Explicitly, for a $^8Li^+$ ion implanted at time $t'$, the spin polarization at time $t > t'$ follows:

$$R(t, t') = \exp\{-[\lambda(t - t')]^{\beta}\}, \tag{1}$$

where $\lambda \equiv 1/T_1$ is the relaxation rate and $0 < \beta \leqslant 1$ is the stretching exponent. We find this to be the simplest model that fits the data well (without overparametrizing it) across all temperatures and fields. Using Eq. (1) convoluted with the 4-s beam pulse [49,50], SLR spectra grouped by magnetic field $B_0$ and implantation energy $E$ were fit simultaneously with a shared common initial asymmetry $A_0(B_0, E)$. Note the statistical uncertainties in the data are strongly time dependent and accounting for this is crucial in the analysis. To find the global least-squares fit, we used custom C++ code leveraging the MINUIT [60] minimization routines implemented within ROOT [61]. The fit quality is good in each case ($\tilde{\chi}^2_{\text{global}} \approx 1.02$) and a subset of the fit results are shown in Fig. 2 as solid black lines. The large values of $A_0$ extracted from the fits (∼10% for $B_0 \geqslant 2.20$ T and ∼16% for $B_0 \leqslant 20$ mT) are consistent with the full beam polarization, implying that there is no appreciable missing fraction due to a very fast relaxing component. The $A_0$ values determined from these fits are used to normalize the spectra in Fig. 2. For all the fits, the stretching exponent $\beta \approx 0.5$, with a weak temperature dependence: in high field, decreasing slightly at temperatures below ∼200 K.

The resulting values of $1/T_1$ are shown in Fig. 3. Consistent with the qualitative behavior of the data, $1/T_1$ is relatively slow at high fields, but both temperature and field

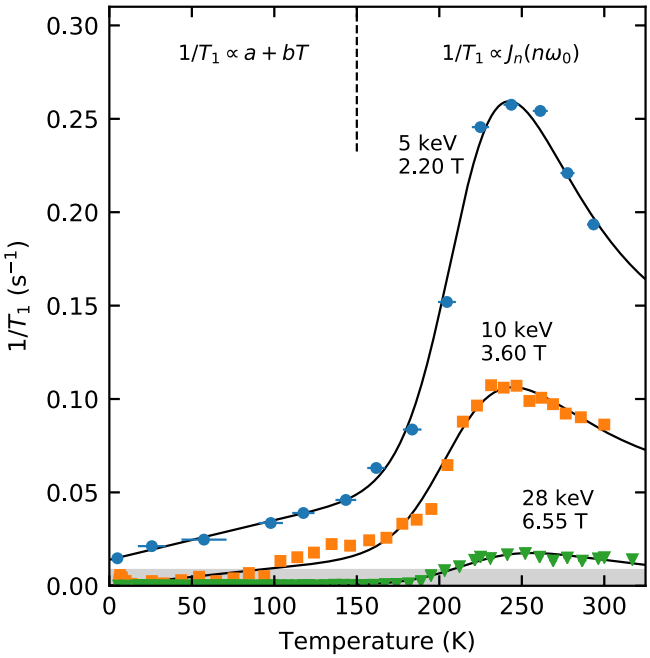


FIG. 3. The spin-lattice relaxation rate for $^8$Li in $Bi_2Te_2Se$ at high magnetic fields with $B_0 \parallel (001)$ using a stretched exponential analysis. $1/T_1$ is strongly field dependent, increasing with decreasing magnetic field, but also increases nonmonotonically with temperature. At each field, a clear $1/T_1$ maximum can be identified where the average fluctuation rate of the dynamics inducing relaxation matches the $^8$Li Larmor frequency. The solid black lines are fits to the model in Eqs. (2)–(4), consisting of a linear $T$ dependence with a nonzero intercept and a term due to ionic diffusion. The highlighted gray region denotes the lower limit of measurable $1/T_1$ due to the $^8$Li probe lifetime.

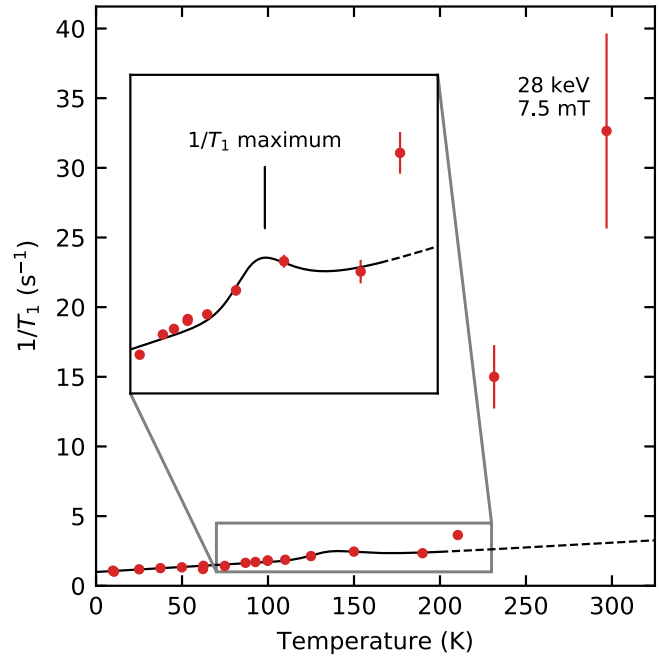


FIG. 4. Temperature dependence of the $^8Li^+$ $1/T_1$ in $Bi_2Te_2Se$ at low magnetic field [7.5 mT $\perp$ (001)]. The relaxation rate is orders of magnitude larger than at high fields, with both a larger apparent $T$-linear slope and intercept. There is some evidence of a small $1/T_1$ peak (see inset) near ~150 K superposed on the dominant linear dependence. Above 200 K, $1/T_1$ increases substantially, suggestive of another relaxation mechanism absent at higher fields.

dependent. Although the data also vary in implantation energy, the differences are primarily due to the applied field. At the highest field, 6.55 T, the relaxation is extremely slow and near the measurable limit imposed by the $^8$Li lifetime (gray region in Fig. 3). As the field is lowered, $1/T_1$ increases, and its temperature dependence is clearly nonmonotonic. Below ~150 K, $1/T_1$ increases approximately linearly with $T$, with a field-dependent slope and $T \to 0$ intercept. At higher temperatures, pronounced $1/T_1$ peaks are observed, whose maxima positions $T_{max}$ are field dependent. As $B_0$ is lowered, $T_{max}$ shifts to slightly lower temperatures, with a more dramatic change when the field is decreased to mT (see Fig. 4).

### B. Modeling $T_1(T, \omega_0)$

We now consider a model of the temperature dependence of the measured $1/T_1$. We interpret the relaxation peak as a Bloembergen-Purcell-Pound (BPP) peak [37], where the rate of a fluctuating interaction with the nuclear spin sweeps through the Larmor frequency $\omega_0 = \gamma B_0$ at the rate peak [37–39]. As we discuss in more detail below, we attribute this fluctuation to diffusive motion of interstitial $^8Li^+$ in the vdW gap between quintuple layers in BTS. It is clear that the peaked relaxation adds to an approximately linearly temperature-dependent term, reminiscent of Korringa relaxation characteristic of NMR in metals [21,22], and probably of electronic origin. Based on this, we use the following model:

$$1/T_1 = a + bT + c(J_1 + 4J_2). \quad (2)$$

The first two terms in Eq. (2) account for the linear $T$ dependence $\lambda_e \equiv a + bT$ and the remaining terms $\lambda_{diff} \equiv c(J_1 + 4J_2)$ describe the peak. $\lambda_{diff}$ consists of a coupling constant $c$ proportional to the mean-squared transverse fluctuating field and the $n$-quantum NMR spectral density functions $J_n$ [39]. In this context, $J_n$ is a frequency-dependent function peaked at $T_{max}$, which occurs when the fluctuation rate driving relaxation matches $\sim n\omega_0$. While the choice of a precise form of $J_n$ depends in detail on the dynamics, we use the empirical expression of Richards [38], which gives the correct asymptotic limits for relaxation produced by 2D fluctations [62], originating, for example, from diffusion of $^8Li^+$ confined to the vdW gap. Explicitly [38],

$$J_n \approx \tau_c \ln[1 + (n\omega_0\tau_c)^{-2}], \quad (3)$$

where $\omega_0$ is the Larmor frequency, and $\tau_c$ is the correlation time, assumed to follow an Arrhenius temperature dependence:

$$\tau_c^{-1} = \tau_0^{-1} \exp[-E_A/(k_B T)], \quad (4)$$

where $\tau_0^{-1}$ and $E_A$ are the prefactor and activation energy, respectively, with $T$ and $k_B$ retaining their usual meanings of the absolute temperature and Boltzmann constant.

Fits of the $1/T_1$ data to the model given by Eq. (2) with Eqs. (3) and (4) are shown in Figs. 3 and 4 as solid black lines, clearly capturing the main features. While the kinetic

TABLE I. Results from the analysis of the $1/T_1$ relaxation peaks in Figs. 3 and 4 using Eqs. (2)–(4). Here, $\measuredangle$ denotes the orientation of the $Bi_2Te_2Se$ trigonal $c$ axis with respect to the applied field $B_0$ and $E$ is the $^8Li^+$ implantation energy. Values for the coupling constant $c$, prefactor $\tau_0^{-1}$, and activation energy $E_A$ are indicated. For comparison, the kinetic parameters extracted from fitting $\omega_0(T_{\max})$ to Eq. (4) in Fig. 8 (described in Sec. IV A) are shown in the bottom row. The good agreement in these values, independent of the analysis details, indicates a single common dynamic process. Differences in the parameter pairs $\tau_0^{-1}$ and $E_A$ may be attributed to the empirical Meyer-Neldel rule [63].

| $B_0$ (T) | $\measuredangle$ | $E$ (keV) | $c$ ($10^6$ s$^2$) | $\tau_0^{-1}$ ($10^{12}$ s$^{12}$) | $E_A$ (eV) |
|---|---|---|---|---|---|
| 6.55 | $\parallel$ | 28 | 1.88(2) | 1.02(13) | 0.156(3) |
| 3.60 | $\parallel$ | 10 | 5.08(10) | 0.7(2) | 0.153(6) |
| 2.20 | $\parallel$ | 20 | 2.86(4) | 28(7) | 0.235(5) |
| 2.20 | $\parallel$ | 5 | 7.23(16) | 1.2(5) | 0.173(9) |
| 0.0075 | $\perp$ | 28 | 0.07(1) | 1 | 0.164(3) |
| | | | | 0.8(3) | 0.185(8) |

parameters determining the position and shape of the SLR peaks varied somewhat at different fields (see Table I), good overall agreement was found from this analysis, and we consider the details further below in Sec. IV A. As anticipated, the slope and intercept of $\lambda_e$ were both strongly field dependent. At low fields, the intercept $a$ is quite large and varies as $\omega_0^{-2}$ (Fig. 5), behavior characteristic of relaxation due to host nuclear spins. Just as in the case of $^8$Li in $NbSe_2$ [55], this field dependence can be described by a simple BPP model [37]: $1/T_1 \propto \bar{C}_0^2[2\tau_c/(1+\omega_0^2\tau_c^2)]$, where $\bar{C}_0^2$ is a coupling constant related to the fluctuating field from host nuclear dipoles. A fit to this model, shown as a solid red line in the upper panel in Fig. 5, yields $\bar{C}_0^2 = 1.5(3)\times 10^6$ s$^{-2}$ and $\tau_c = 3.2(7)\times 10^{-5}$ s. We note that the magnitude of $\bar{C}_0^2$ is compatible with the observed $^8$Li resonance linewidth, discussed in Sec. III C, and that $\tau_c$ is remarkably close to the $^{209}$Bi NMR $T_2$ time in $Bi_2Se_3$ [26]. It is, however, not clear whether the intercept at 2.20 T is a remnant of this low-field relaxation, or is due to an electronic mechanism [64]. In any case, it is small and we will not consider it further. In contrast, the slope $b$ varies as $\omega_0^{-1.5}$ with a pronounced anisotropy between orientations (Fig. 5). We return to these points below in Sec. IV B.

### C. Resonance spectra

We now turn to the $^8$Li resonance in BTS. Typical spectra at high field are shown in Fig. 6. Consistent with a noncubic crystal, the $^8$Li NMR is quadrupole split (as described in Sec. II A). This is confirmed by the helicity-resolved spectra (see Fig. 11 in Appendix B) which show opposite satellites in opposite helicities [33]. The EFG that produces the splitting is characteristic of the $^8$Li site in the crystal. From the spectra, it is relatively small, on the order of a few kHz. In addition, a second unsplit line is evident near the midpoint of the quadrupole pattern. This line must be due to a distinct $^8$Li site with a small, unresolved quadrupolar splitting. A similar unsplit resonance was observed in the vdW layered material $NbSe_2$ [54], which was thought to originate from implanted $^8Li^+$ stopped at an interstitial site within the vdW gap.

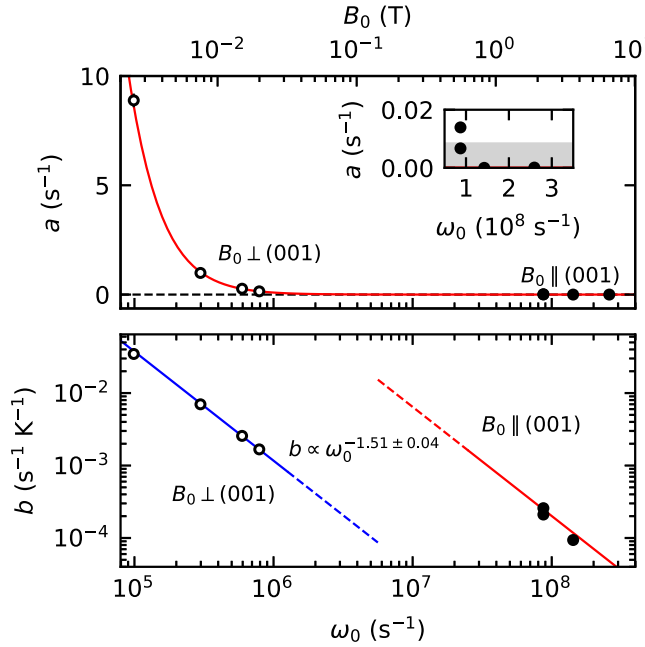


FIG. 5. Field dependence of the intercept $a$ and slope $b$ describing the low-temperature electronic relaxation in Eq. (2). (Top panel) The $T \to 0$ intercept of $1/T_1$ falls with increasing field as $1/\omega_0^2$, behavior consistent with a low-field relaxation due to fluctuating host lattice nuclear spins [55]. The solid red line indicates a fit to a simple BPP model [37], yielding a coupling constant $\bar{C}_0^2 = 1.5(3)\times 10^6$ s$^{-2}$ and correlation time $\tau_c = 3.2(7)\times 10^{-5}$ s$^{-1}$, the latter being remarkably close to the $^{209}$Bi NMR $T_2$ time in $Bi_2Se_3$ [26]. The inset shows a zoom of the small high-field intercepts, at the lower limit measurable due to the $^8$Li probe lifetime highlighted in gray. (Bottom panel) Field dependence of the low-temperature slope of $1/T_1$, exhibiting a strong orientation dependence, but a common field dependence $\propto \omega_0^{-1.5}$, indicated by the solid colored lines.

This evidence for two sites suggests that our single-component relaxation model in Sec. III B is too simple. However, more complicated relaxation functions suffer from overparametrization, and we have retained the single stretched exponential to represent the overall average relaxation of $^8$Li in BTS.

The resonance was found to evolve substantially with temperature, as shown in Fig. 6. Here, the spectra have been normalized to the off-resonance steady-state asymmetry to account for the variation of intensity due to SLR [52]. While it is apparent that the satellite intensities and splitting remain nearly temperature independent, the amplitude of the central line increases significantly above ~100 K, becoming the dominant feature by room temperature. Additionally, a small shift in the resonance center-of-mass frequency can be seen, increasing in magnitude with decreasing temperature.

To quantify these observations, we now consider a detailed analysis, noting first that the scale of the quadrupolar splitting is given by the quadrupole frequency [36]

$$\nu_q = \frac{e^2qQ}{8h}. \tag{5}$$

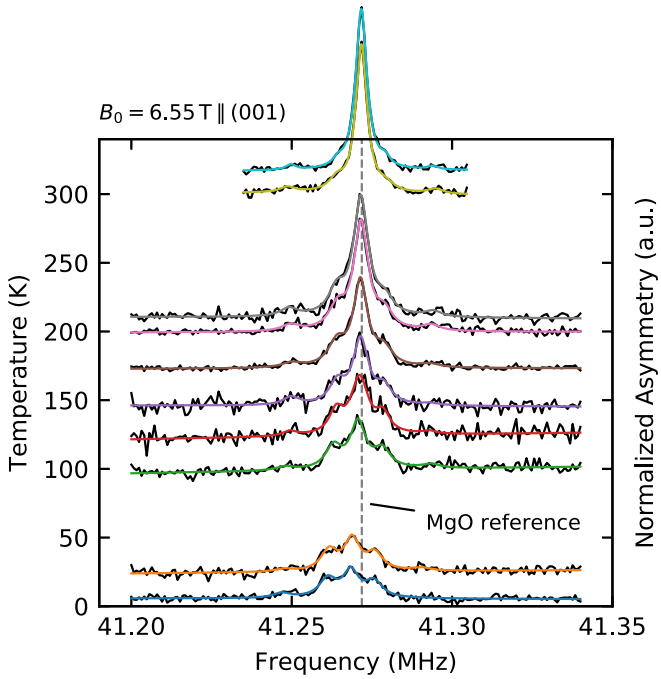


FIG. 6. $^8$Li NMR spectra in $Bi_2Te_2Se$ with 6.55 T ∥ (001) shown as solid black lines. The vertical scale is the same for all the spectra, but the baselines are offset to match the absolute temperature indicated on the left. The spectra reveal a small, temperature-independent quadrupole splitting, centered about an unsplit Lorentzian line, whose amplitude grows above 100 K, becoming the dominant feature at higher temperatures. The solid colored lines are global fits to a sum of this Lorentzian plus $2I = 4$ quadrupolar satellites of the quadrupole split resonance (see text for further details). The reference frequency, determined by the $^8$Li resonance position in MgO (100) at room temperature, is indicated by the vertical dashed gray line. Note the small negative shift of the $Bi_2Te_2Se$ resonances as the temperature is lowered.

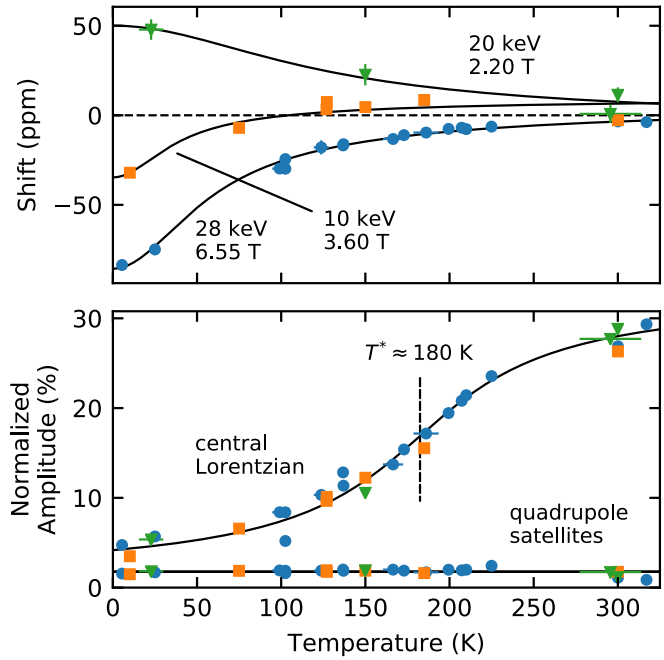


FIG. 7. Fit results for $^8$Li resonance in $Bi_2Te_2Se$ at high field with $B_0 \parallel (001)$, following the fitting procedure described in the text. The upper panel shows the resonance shift $\delta$ relative to MgO. Above ∼150 K, the shift is nearly field independent and scattered about zero; however, at lower temperatures, the trends at each field diverge, revealing a field-dependent shift whose magnitude is maximized at the lowest temperatures. The lower panel shows the change in amplitude of the central Lorentzian and quadrupole satellites (averaged over all four lines), normalized by the off-resonance baseline [52]. The amplitude of the unsplit line grows above ∼100 K, contrasting the temperature independence of the quadrupole satellite amplitudes. The inflection point $T^*$ of this trend is indicated by the dashed vertical black line. The solid black lines are drawn to guide to the eye.

As the splitting is small (i.e., $\nu_q \ll \nu_0$), the satellite positions are given accurately by the first-order expression [36]

$$\nu_i = \nu_0 - n_i \nu_q f(\theta, \phi, \eta), \tag{6}$$

where $n_i = \pm 1$ ($\pm 3$) for the inner (outer) satellites. The angular factor

$$f(\theta, \phi, \eta) = \tfrac{1}{2}(3\,\cos^2\theta - 1 + \eta\,\sin^2\theta\,\cos 2\phi) \tag{7}$$

scales the splittings according to the polar ($\theta$) and azimuthal ($\phi$) angles between the external field and the EFG principal axis. The parameter $\eta \in [0, 1]$ is the EFG asymmetry, which for axially symmetric sites is zero. From $\nu_0$, we additionally calculate the frequency shift $\delta$ in parts per million (ppm) using

$$\delta = 10^6\left(\frac{\nu_0 - \nu_{\mathrm{MgO}}}{\nu_{\mathrm{MgO}}}\right), \tag{8}$$

where $\nu_{\mathrm{MgO}}$ is the reference frequency position in MgO at 300 K with $B_0 \parallel (100)$ [51].

The helicity-resolved spectra were fit using the quadrupole splitting above with $\nu_0$ and $\nu_q$ as free parameters, in addition to linewidths and amplitudes. Similar to the SLR spectra in Sec. III A, a global fitting procedure was used by way of ROOT's [61] implementation of MINUIT [60]. The two helicities of each spectrum were fit simultaneously with resonance positions and widths as shared parameters. The fits were constrained such that the center-of-mass frequency $\nu_0$ was shared between the unsplit Lorentzian and quadrupole satellites. Any difference in center of mass of the split and unsplit lines was too small to measure accurately, and the two lines shift in unison with temperature, as can be seen in Fig. 6. In addition, we assume the EFG principal axis is along the $c$ axis and $\eta = 0$, making the angular factor unity. This assumption does not affect accurate extraction of the splitting frequency, but precludes unambiguous identification of the EFG tensor elements. Based on a simple point charge model of the lattice (see Appendix C), all reasonable interstitial $^8Li^+$ sites retain the threefold rotation axis of the hexagonal unit cell, supporting this simplification. The change in satellite splittings from preliminary measurements at low field with $B_0 \perp c$ are consistent with an EFG principal symmetry axis parallel to $c$.

The main parameters extracted from this analysis are shown in Fig. 7. Consistent with the two main qualitative features of the spectra, both the amplitude and shift show substantial changes with temperature. In the top panel of

Fig. 7, above ∼150 K, the shift is nearly field independent and centered around ∼0 ppm. Shifts of this magnitude are difficult to quantify accurately and the scatter in the values is of the same order as systematic variations in the line position, making differences of this order not very meaningful. In contrast, at lower temperatures, the shift trends for each field diverge, revealing a significant field-dependent shift whose magnitude is maximized at the lowest temperature.

The changes in amplitude of the central Lorentzian and quadrupole satellites (averaged over all four lines), normalized by their off-resonance baseline [52], appear in the bottom panel of Fig. 7. Consistent with Fig. 6, the amplitude of the unsplit line grows above ∼100 K and approaches saturation near room temperature, in contrast to the temperature insensitivity of the satellite amplitudes. From the smooth growth of the unsplit line amplitude, we identify the inflection point $T^* \approx 180$ K of the trend, as indicated in Fig. 7. The other spectral parameters are nearly independent of temperature. The linewidths are about ∼6 kHz, with the central Lorentzian narrowing slightly with increasing $T$. This narrowing is likely the cause of its increase in amplitude. Similarly, $\nu_q \approx 7.4$ kHz was characteristic of the splittings over the entire measured temperature range.

Based on these results at the lowest measured temperatures, where dynamic contributions to the resonance are absent, we estimate a 1:1 relative occupation for $^8Li^+$ in the two sites. Note, however, that changes in amplitude, up to our highest measured temperature 317 K, are inconsistent with a site change, where the growth of one amplitude is at the expense of the other [45].

## IV. DISCUSSION

With the main results presented in Sec. III, the remaining discussion is organized as follows: In Sec. IV A, we consider the dynamics causing the high-temperature $1/T_1$ peaks, while Sec. IV B considers the electronic properties of BTS giving rise to relaxation and resonance shifts at low temperature.

### A. High-temperature lithium-ion diffusion

The most likely source of the relaxation at high temperatures is diffusive motion of $^8Li^+$. While we cannot rule out some local stochastic motion within a cage, or motion of another species in the lattice, given the demonstrated ability to chemically insert Li at room temperature in isostructural bismuth chalcogenides [65,66], we expect a low barrier to interstitial diffusion for any implanted $^8Li^+$ in the vdW gap. Stochastic motion causes the local magnetic field and EFG to become time dependent causing relaxation [37,38]. From the SLR, we can thus obtain information on the kinetic parameters of the diffusion. From the model of $1/T_1(T)$ introduced in Eq. (2) from Sec. III B, we obtain the kinetic parameters listed in Table I. The success of the model is demonstrated by the good self-agreement in the barrier $E_A$ and prefactor $\tau_0^{-1}$, indicating that an activated dynamic process with a 2D spectral density provides a single common source for the observed $\lambda_{\text{diff}}$. Thus, the correlation rate $\tau_c^{-1}$ in Eq. (4) represents the atomic hop rate $\tau^{-1}$. The small barrier, on the order of ∼0.2 eV, is consistent with expectations for an isolated interstitial ion, where Coulomb $Li^+$-$Li^+$ repulsion is negligible. Similarly, the $\tau_0^{-1}$'s on the order of $\sim 10^{12}$ s$^{-1}$ are compatible with typical optical phonon frequencies, as is often the case for mobile ions in a lattice. The relatively small deviations in $E_A$ and $\tau_0^{-1}$ obtained at different fields may be ascribed to the empirical Meyer-Neldel rule, where $\tau_0^{-1}$ increases exponentially with increasing $E_A$, as is often observed for related kinetic processes [63].

In general, the exponent appearing in $J_n$ from Eq. (3) can vary from -1 to -2 [67], with deviations from -2 reflecting correlated dynamics that can arise from, for example, Coulomb interactions with other ions acting to bias the probe ion's trajectory. Such correlations affect the shape of the $1/T_1$ peak, yielding a characteristic asymmetry with a shallower slope on the low-$T$ side. In contrast, the high symmetry about $T_{\text{max}}$ is consistent with uncorrelated fluctuations driving relaxation, as expected for isolated $^8$Li undergoing direct interstitial site-to-site hopping.

As further confirmation of the appropriateness of the form of $J_n$, we considered an alternative approach agnostic to these details. At each field, we determined the temperature $T_{\text{max}}$ of the $1/T_1$ peak using a simple parabolic fit (after removal of the $T$-linear contribution). This approach has the advantage that it does not rely on any particular form of $J_n$, and we recently used it to quantify diffusion of isolated $^8Li^+$ in rutile $TiO_2$ [68]. Finally, for each $T_{\text{max}}$ we assumed $\tau_c^{-1}$ matches the Larmor frequency $\omega_0$. The results are shown in the Arrhenius plot in Fig. 8, where the linearity of the data, spanning three orders of magnitude, demonstrates the consistency of the approach. The Arrhenius fit shown yielded an activation energy $E_A = 0.185(8)$ eV and prefactor $\tau_0^{-1} = 8(3) \times 10^{11}$ s$^{-1}$, in good agreement with the values from the analysis using the 2D $J_n$. Noting that this result lies in the middle of range reported in Table I, we take it as the best determination of the $^8Li^+$ hop rate.

Another well-known signature of diffusion in NMR is motional narrowing. When the diffusive correlation rate exceeds the characteristic static frequency width of the line, the local broadening interactions are averaged and the line narrows. In the context of dilute interstitial diffusion in a lattice, the primary quadrupolar interaction may, however, not be averaged to zero since, in the simplest case, each site is equivalent and characterized by the same EFG. We observe a slight narrowing and a large enhancement in the amplitude of the unsplit resonance with an onset in the range 100–120 K, consistent with where the extrapolated $\tau_c^{-1}$ would be in the kHz range of the linewidth. With the CW resonance measurement, we often find the change in amplitude is more pronounced than the width [69].

Using the $^8Li^+$ hop rate from above, we convert $\tau^{-1}$ to diffusivity via the Einstein-Smoluchowski expression

$$D = f\frac{l^2}{2d\tau}, \tag{9}$$

where $l$ is the jump length, $d = 2$ is the dimensionality, and $f$ is the correlation factor, assumed to be unity for direct interstitial diffusion, to compare with other measurements of interstitial ionic diffusion in related materials. Using

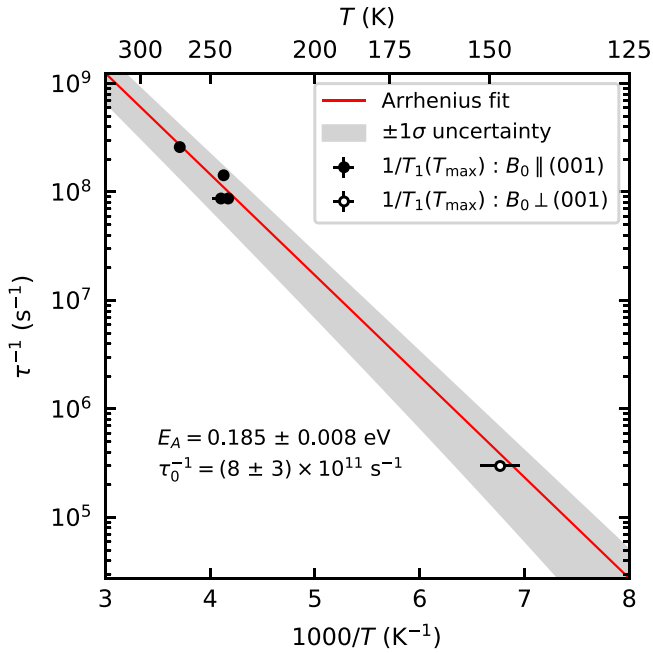


FIG. 8. Arrhenius plot of the $^8$Li fluctuation rate extracted from the NMR frequency-dependent positions of $1/T_1(T_{max})$ in Figs. 3 and 4. The solid red line is a fit to Eq. (4) with the activation energy $E_A$ and prefactor $\tau_0^{-1}$ indicated in the inset and the fit's $\pm 1\sigma$ uncertainty band is highlighted in gray. The kinetic parameters extracted from this minimally model-dependent analysis are in good agreement with those obtained from fits of the $1/T_1$ data to Eqs. (2)–(4), given in Table I.

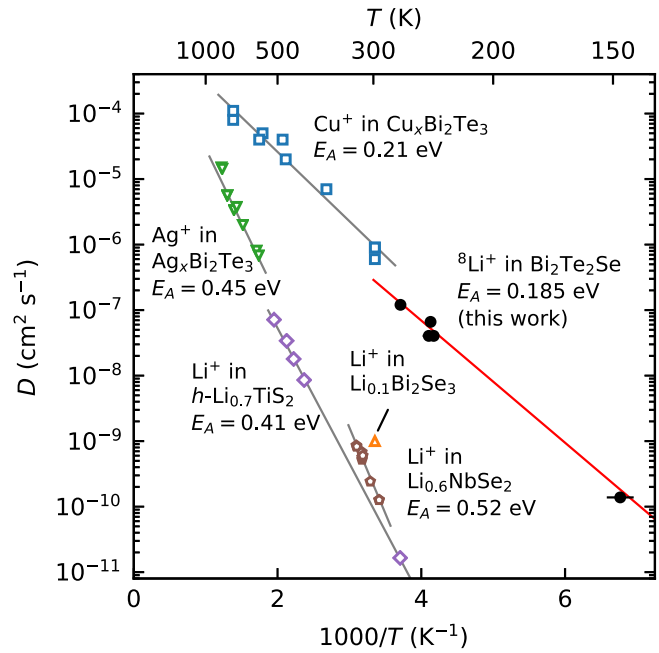


FIG. 9. Arrhenius plot of the diffusion coefficient $D$ for $^8$Li$^+$ in $Bi_2Te_2Se$. Values for $D$, shown in black, were estimated using the Einstein-Smoluchowski expression [Eq. (9)], taking $f = 1$, $d = 2$, and $l = 4.307$ Å, with the values of $\tau^{-1}$ taken from Fig. 8. For comparison, diffusion coefficients for Li$^+$ [65,72,74], Ag$^+$ [71], and Cu$^+$ [70,73] in structurally related materials are also included. It is clear that the diffusivity of isolated $^8$Li$^+$, free from repulsive Li$^+$-Li$^+$ interactions, is exceptional, significantly exceeding that in the well-known fast ion conductor $h$-Li$_x$TiS$_2$ [74,75].

$l \approx 4.307$ Å, the distance between neighboring $3b$ sites in the vdW gap in the ideal BTS lattice (see Fig. 12 in Appendix C), we estimate $D$ for $^8$Li$^+$, finding a value on the order of $10^{-7}$cm$^2$s$^{-1}$ at 300 K. An Arrhenius plot comparing the diffusivity of $^8$Li$^+$ in BTS with other cations in structurally related materials [65,70–74] is shown in Fig. 9. Note that most of these diffusion coefficients were determined using either radiotracer [70,71] or transient electrochemical [65,72,73] techniques. For $h$-$Li_{0.7}TiS_2$, we used the Li$^+$ hop rate determined by $^7$Li NMR [74] and Eq. (9), taking $f = 1$, $d = 2$, and $l = 2.14$ Å (the distance between $1b$ and $2d$ sites) [75].

It is clear that the mobility of isolated $^8$Li$^+$ is exceptional; our estimate for $D$ greatly exceeds that of lithium in the well-known fast ion conductor $h$-Li$_x$TiS$_2$ [74,75]. Similarly, the lithium diffusion coefficient in lithium intercalated $Bi_2Se_3$ is considerably slower [65], possibly due to Li$^+$-Li$^+$ interaction. Interestingly, the mobility of Cu in isostructural $Bi_2Te_3$ is also extremely high, as revealed by $^{64}$Cu radiotracer [70] and electrochemical methods [73]. Lastly, we note that similarly large-$D$ values were reported recently for $^8$Li$^+$ in the one-dimensional ion conductor rutile $TiO_2$ [68] and we speculate that the exceptional mobility may be generic for *isolated* Li$^+$ (i.e., at infinitely dilute concentrations) in ion-conducting solids. It would be interesting to test this conjecture against detailed *ab initio* calculations. Understanding the mobility of dilute intercalates, a simple theoretical situation difficult to interrogate experimentally, remains of fundamental interest [76].

### B. Low-temperature electronic properties

We turn now to the low-temperature results, below the diffusion-related peak, in the range 5 to 150 K. The diffusive contribution to the relaxation rate is falling exponentially with reduced temperature below the peak, and the remaining low-temperature relaxation must thus have a distinct origin. In this regime, the relaxation rate is linear in $T$, with a slope that is significantly field dependent. In this range, there is also a $T$-dependent resonance shift that is also field dependent.

In metals, the dominant features of NMR (and $\beta$-NMR) are due to coupling between the conduction electron and nuclear spins, giving rise to the Korringa $T$-linear $1/T_1$ and a $T$-independent Knight shift proportional to the Pauli susceptibility [21,22]. The apparent Korringa-type dependence in Figs. 3 and 4 is thus surprising since ideal BTS is a narrow-gap semiconductor, with an energy gap $E_g \approx 0.3$ eV [10]. In comparison to metals, NMR in semiconductors is much less well known, largely because the coupling to the electron spins is much less universally dominant, and often other channels, such as phonons, compete with electronic effects and complicate the interpretation (e.g., in elemental Te [77] and InSb [78], with similar $E_g$ to BTS). However, while calculations and experiments agree on $E_g$ in BTS [10,14], it is abundantly clear from both experiment [79] and theory [9,80] that it is unlikely to exist as an intrinsic semiconductor. Rather, it is significantly self-doped by native defects, such as chalcogenide vacancies (donor) and Bi/Te antisite defects

(acceptor). Among the tetradymites, BTS is relatively highly insulating, but this does not indicate a paucity of native defects, but rather a coincidental near compensation between the $n$ and $p$ types. Brahlek *et al.* have made the point that these materials are, in fact, so highly doped that they are metallic, but are poor conductors due to disorder [81]. Such disorder is clearly evident in our data, contributing to the stretched exponential character of the spin relaxation and the line broadening.

The origin of the linearity of the Korringa law is evident from a derivation based on a Fermi golden rule approach to the spin-flip scattering of conduction electrons by the hyperfine interaction with the nuclear spin. The sum over electron momenta when converted to an integral over energy yields

$$\frac{1}{T_1} = \frac{2\pi}{\hbar} A^2 \int \rho^2(E) f(E)[1 - f(E)]\, dE, \qquad (10)$$

where $A$ is the hyperfine coupling energy, $f(E)$ is the Fermi-Dirac distribution, $\rho(E)$ is the electronic density of states, and the integral is over all electron energies in the conduction band. In a broad band degenerate metal, where the Fermi level $E_F \gg k_B T$, the density of states $\rho(E)$ is practically constant over the range where the Fermi factor is nonzero, and the integral is given to an excellent approximation by

$$\frac{1}{T_1} = \frac{2\pi}{\hbar} A^2 \rho^2(E_F) k_B T. \qquad (11)$$

The Korringa slope is thus determined by the square of the product of $A$ and $\rho(E_F)$. In fact, on inspection of the $^8$Li $\lambda_e$ in BTS, we find it comparable to wide-band metals with vastly higher carrier densities [45,52,54,56,82–85]. While the coupling $A$ for implanted $^8Li^+$ in BTS is not known, it is unlikely to compensate for the much lower $\rho(E_F)$, to yield a comparable Korringa slope. Note that the Korringa law is remarkably robust to disorder and, for example, applies in the normal state of the alkali fullerides where the mean-free path is comparable to the lattice constant (the Ioffe-Regel limit) [86]. However, in highly disordered metals, the slope is strongly enhanced [87–89]. Such an enhancement may account for the substantial slope we observe. However, Eq. (10) indicates that if $\rho(E)$ has significant structure on scales comparable to $k_B T$, as it might in a narrow impurity band, its detailed form and nondegeneracy can render the $T$ dependence nonlinear [90], as found, for example, near the metal-insulator transition (MIT) in doped silicon [91]. Thus, the evident linearity is still surprising. Moreover, in metals, the Korringa slope does *not* depend on magnetic field.

In doped Si, near the MIT, a field dependence of the enhanced Korringa slope has been found at mK temperatures [92], where it was attributed to the occurrence of uncompensated localized electron spins, probably on some subset of more isolated neutral P donors. Such moments are also evident in the NMR of the dopant nuclei [93]. However, in BTS (in contrast to Si), due to the high dielectric constant and low effective mass, *magnetic carrier freeze-out* [94,95] may account for the diminished slope at high fields. In this case, the field localizes the carriers so they no longer participate in the conduction band, correspondingly reducing the Korringa slope. This may account, in part, for the significant positive magnetoresistance in BTS [12,96]. Similarly, the field- and temperature-dependent shifts in Fig. 7 may reflect a constant (diamagnetic) contribution (cf. the $^{125}$Te shift [27]), in addition to a positive hyperfine field related to the carriers, which diminishes with localization. However, the localized electrons may well provide additional (more inhomogeneous) relaxation and resonance broadening. We know of no case where NMR has been used to study magnetic freeze-out. In order to test this idea, it will be essential to compare results on different samples of BTS and related materials (e.g., Ca-doped $Bi_2Se_3$).

Above, we only considered bulk origins for the $\lambda_e$. While we do not expect any direct coupling to the topological surface state at the implantation energies used, it is important to consider the effects of band bending at the surface. If the bulk electronic bands are bent downward at the surface, a conventional 2D electron gas may be stabilized [29]. Metallic screening will confine this surface region to a few nm from the surface. In the opposite case, upward bending makes the surface region more insulating, and the dielectric screening is much weaker, producing a depletion region on the scale of $\mu$m, as has been demonstrated by ionic liquid gating [97]. In the latter case, the acceptor band is depopulated by the surface dipole. Calculations suggest this is not the case [98], but there is substantial evidence for time-dependent band bending from ARPES [18]. Generally, this downward bending is found to produce a more metallic surface. With its exposure to air prior to the measurements, we assume that our sample's surface is passivated and is metallic, typical of an "aged" surface, so we can safely neglect possible depth dependence to the carrier concentration at the implantation energies used. This is consistent with the absence of an appreciable implantation energy dependence in $\lambda_e$ at 2.20 T (not shown).

We have, so far, focused exclusively on the interaction between $^8$Li and the electron *spins*. We should also consider its interaction with their orbital currents. Note that at 100 K, $1/T_1$ in BTS is comparable to semimetallic bismuth [53], with a similar carrier density, but a much longer mean-free path. In Bi, due to its strong orbital diamagnetism, we suggested that orbital fluctuations might be responsible for the fast relaxation of $^8$Li and its concentration dependence in $Bi_xSb_{1-x}$ solid solutions [53]. This mechanism is due to fluctuating electronic currents, so it is naturally related to the conductivity $\sigma$. Specifically [99],

$$\left(\frac{1}{T_1}\right)_{\text{orb}} \propto k_B T \int \frac{\text{Re}\{\sigma_\perp(q, \omega_0)\}}{q^2}\, d^3q, \qquad (12)$$

where $\sigma_\perp(q, \omega)$ is the generalized wave vector ($q$) and frequency-dependent conductivity transverse to the nuclear spin. Clearly, this relaxation is enhanced by higher conductivity; however, in metals, it has long been recognized that orbital relaxation is usually much weaker than the spin-related Korringa relaxation discussed above.

In a layered conductor, the hyperfine coupling $A$ for interstitial $^8$Li can be particularly weak (e.g., $NbSe_2$ [54]). In these circumstances, it is possible that orbital relaxation will dominate. Unlike the contact coupling, orbital fields fall as $1/r^3$, where $r$ is the distance between the probe spin and the fluctuating current, so all nuclei in the material, and potentially even nuclei in close proximity, will sense spatially

extended orbital fluctuations. For example, this mechanism has been studied as a proximal source of decoherence in spin-based qubit devices [100]. Lee and Nagaosa have explicitly considered the case of orbital relaxation in a 2D layered metal [101]. They find a weak logarithmic singularity in $1/T_1$ in the clean limit that is cut off by a finite mean-free path [102]. Similar to the Korringa rate, the orbital relaxation rate is linear in $T$ for a broad band metal. Recently, this approach was generalized to the case of massive Dirac-type electrons in 3D, appropriate to semimetallic $Bi_{1-x}Sb_x$ [99,103]. They find $T$-linear relaxation when the chemical potential is outside the gap [99], but within the gap, an anomalous relation that is explicitly field dependent via the NMR frequency $\omega_0$ is obtained, where $\lambda_{\rm orb} \propto T^3 \ln(2k_BT/\hbar\omega_0)$. While this is not what we find, it does suggest that if orbital relaxation is effective here, it may exhibit some unexpected field dependence in the inhomogeneous metallic state hypothesized for the tetradymites [104]. Similarly, orbital current fluctuations will almost certainly be accompanied by a fluctuating charge distribution (and hence EFG), giving rise to a quadrupolar relaxation in addition to the magnetic orbital relaxation. This has been considered explicitly for Dirac electrons in 3D, and it was concluded that the quadrupolar contribution was negligible [99]. While this result probably does not apply directly here, it suggests a theory for the relaxation in BTS could focus on a purely magnetic mechanism.

In fact, some features of our data do suggest the importance of orbital effects. One is the similarity of shifts of the quadrupolar split resonance and the unsplit Lorentzian. If, as seems to be reasonable, these resonances originate in different lattice sites of $^8Li^+$, then one would expect different hyperfine couplings and different (spin) shifts. If the shift is rather orbital in origin with significant contribution from long length-scale currents, one would expect the same shift for any site (and even any nucleus) in the unit cell. In general, however, one would expect both spin and orbital couplings, and nuclei of such different species, such as $^{209}Bi$ or $^8Li$, would likely differ.

We have ruled out a number of possibilities, but we do not have a conclusive explanation of the interesting features of the data at low temperatures. At this point, it is worth noting that conventional NMR in the tetradymite TIs is also characterized by highly variable power-law $T$-dependent relaxation [24,26,105] whose dependence on magnetic field has largely not been explored.

## V. CONCLUSION

Using temperature- and field-dependent ion-implanted $^8Li$ $\beta$-NMR, we studied the high-temperature ionic and low-temperature electronic properties of $Bi_2Te_2Se$. Two distinct thermal regions were found: above ~150 K, the isolated $^8Li^+$ probe undergoes ionic diffusion with an activation energy $E_A = 0.185(8)$ eV and attempt frequency $\tau_0^{-1} = 8(3) \times 10^{11}$ s$^{-1}$ for atomic site-to-site hopping. A comparison of the kinetic details with other well-known $Li^+$ conductors suggests an exceptional mobility of the isolated ion. At lower temperature, field-dependent relaxation and resonance shifts are observed. While the linearity of the spin-lattice relaxation is reminiscent of a Korringa mechanism, existing theories are unable to account for the extent of the field dependence. We suggest that these may be related to a strong contribution from orbital currents or the magnetic freeze-out of charge carriers in the heavily compensated semiconductor. Field-dependent conventional NMR of the stable host nuclei, combined with the present data, will further elucidate their origin.

## ACKNOWLEDGMENTS

We thank R. Abasalti, D. J. Arseneau, B. Hitti, S. Daviel, K. Olchanski, and D. Vyas for their excellent technical support; D. E. Eldridge, Q. Song, and D. Wang for some help with the early measurements and analysis; M. Ogata and J. A. Folk for useful discussions and comments; K. Foyevtsova and P. Blaha for help with the density functional calculations; and O. Prakash for assistance with transport measurements. This work was supported by NSERC Discovery grants to R.F.K. and W.A.M., as well as NSERC CREATE IsoSiM Fellowships to R.M.L.M. and A.C. The crystal growth at Princeton University was supported by the ARO-sponsored MURI on topological insulators, Grant No. W911NF1210461.

## APPENDIX A: IMPLANTATION PROFILES

As mentioned in Sec. II B, $^8Li^+$ implantation profiles in BTS were predicted using the SRIM Monte Carlo code [106]. At each implantation energy, stopping events were simulated for $10^5$ ions, with their resulting histogram representing the predicted implantation profile. From the profiles shown in Fig. 10, we calculate, in the nomenclature of ion-implantation

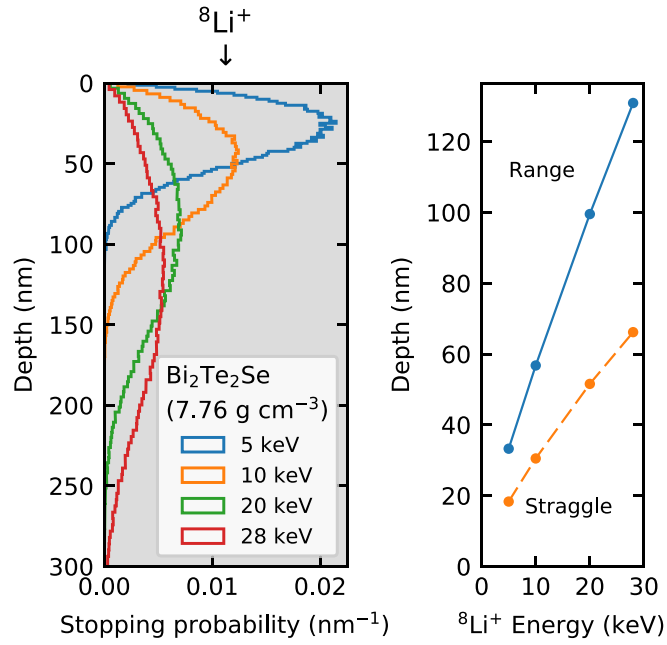


FIG. 10. Stopping distribution and range for $^8Li^+$ implanted in $Bi_2Te_2Se$ calculated using the SRIM Monte Carlo code [106]. The histogram profiles, shown on the left, are generated from simulations of $10^5$ ions. The ion range and straggle at each implantation energy are shown on the right. All measurements in this study correspond to average stopping depths $\gtrsim$30 nm below the crystal surface, well below where the topological surface state is expected to be important.

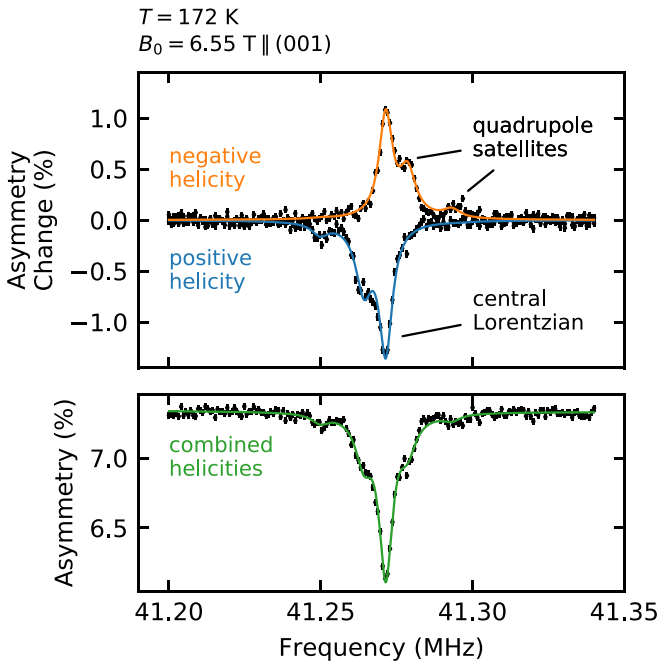


FIG. 11. Typical helicity-resolved $^{8}$Li resonance spectra in $Bi_2Te_2Se$ with 6.55 T ∥ (001), revealing the fine structure of the line. Four quadrupole satellites, split asymmetrically in each helicity about a "central" Lorentzian line, are evident. Note that, in contrast to conventional NMR, the satellite amplitudes are determined primarily by the high degree of initial polarization [48]. The solid colored lines are global fits to a sum of five Lorentzians with positions given by Eqs. (5)–(7) (see Sec. III C for further details). Upon combining helicities, a nearly symmetric line about the resonance center of mass, shown in the bottom panel, is obtained.

literature, the range and straggle (i.e., the mean and standard deviation) at each simulated energy. At the implantation energies used here, 5–28 keV, the incident $^{8}Li^{+}$ ions typically stop on average >30 nm below the crystal surface, depths well below where the TSS is expected to be important.

## APPENDIX B: HELICITY-RESOLVED RESONANCE SPECTRA

Typical helicity-resolved resonance spectra are shown in Fig. 11, demonstrating the two key features in the line's fine structure. A quadrupolar splitting on the order of several kHz, clearly evidenced by the asymmetric shape about the resonance center of mass in each helicity, can be associated with the outermost satellite lines. Note that the satellite intensities are different from conventional NMR and are determined mainly by the high degree of initial polarization, which increases the relative amplitude of the outer satellites [48], with their precise (time-average) values depending on the relaxation details [52]. Second, another significantly smaller quadrupolar frequency can be ascribed to a "central" Lorentzian-type line, analogous to what was observed in the structurally similar $NbSe_2$ [54]. Note that there is no unshifted $m_{\pm 1/2} \leftrightarrow m_{\mp 1/2}$ magnetic sublevel transition, in contrast to spin $I = \frac{3}{2}$ $^{7}$Li. The RF amplitude dependence and the absence of other multiquantum lines indicate that it is also not a multiquantum transition. Instead, it must originate from the overlap of the four unresolved satellites with a small quadrupole splitting [53]. Such a feature, in a noncubic layered crystal (see Fig. 1 in Sec. I), is suggestive that this component originates from $^{8}Li^{+}$ within the vdW gap, where the magnitude of EFGs at interstices are minimized. Resonances of the two helicities can be combined to give an overall average line shape (see bottom inset in Fig. 11), whose evolution with temperature is shown in Fig. 6 from Sec. III C.

## APPENDIX C: $^{8}Li^{+}$ SITES

Here, we consider the stopping sites in more detail. Generally, ion-implanted $^{8}Li^{+}$ occupies high-symmetry crystallographic sites that locally minimize its electrostatic potential. This may include metastable sites that are not the energetic minimum, but have a significant potential barrier to the nearest stable site. While these sites are characteristic of the isolated implanted ion, they may be related to the lattice location of $Li^{+}$ obtained by chemical intercalation.

BTS is structurally similar to the transitional metal dichalcogenides (TMDs) that consist of triatomic layers separated by a vdW gap between chalcogen planes. This spacious interstitial region accommodates many types of extrinsic atoms and small molecules in the form of intercalation compounds [107]. Similarly, a variety of dopants have been intercalated into the tetradymite Bi chalcogenides, such as Cu [73], Ag [108], Au [109], and Zn [110]. Lithium has also been inserted into Bi chalcogenides [65,66,111,112], but the precise sites for $Li^{+}$ in the vdW gap have not been determined [66]. Note that in all these cases, intercalation is at the level of

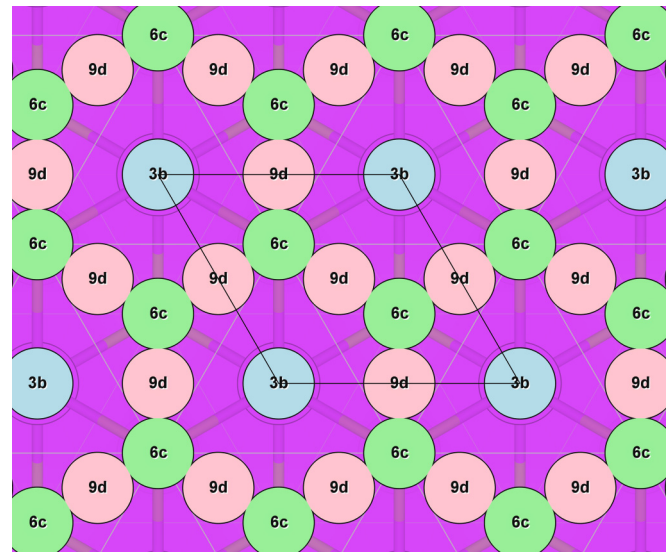


FIG. 12. High-symmetry sites within the van der Waals gap of $Bi_2Te_2Se$, shown as colored circles, in a plane perpendicular to the trigonal $c$ axis. The Wyckoff position is indicated for each site and the boundary of the unit cell is marked by solid black lines. Neighboring 3*b* (blue) sites, enclosed by Te quasioctahedra, are connected indirectly through 6*c* (green) sites with quasitetrahedral Te coordination, and directly through 9*d* (pink) sites of lower symmetry. The structure was drawn using VESTA [20].

atomic %, so that intercalated species certainly interact (e.g., forming "stage" compounds [107]).

Based on this, we expect the lowest-energy site for implanted $^8Li^+$ is within the vdW gap, similar to $NbSe_2$ [54]. Here, the EFGs are likely minimized, yielding a small quadrupole frequency, consistent with the unsplit component of the resonance in Fig. 11. Within the vdW gap, several high-symmetry Wyckoff sites are available (see Fig. 12): the quasioctahedral 3*b* at (0, 0, 1/2); the quasitetrahedral 6*c* at (0, 0, 1/6); and the twofold coordinated 9*d* at (1/2, 0, 1/2). Here, the fractional coordinates correspond to the hexagonal unit cell in Fig. 1 from Sec. I. Neighboring 3*b* sites are connected by direct paths through the 9*d* sites and indirect paths (i.e., dog-leg trajectories) passing through 6*c* sites. The 3*b* site offers by far the largest coordination volume for interstitial $^8Li^+$ and it is reasonable that this is the preferred site in the vdW gap. Indeed, preliminary density functional theory calculations confirm this assignment.

As indicated in Sec. III C, the low-temperature resonances suggest a nearly 1:1 relative occupation of two sites with different EFGs. Noting that, in contrast to the trilayers in TMDs, the QLs in BTS account a much larger volume fraction of the crystal, which leads us to consider possible interstitial sites therein. While interstitial sites within the QL will be characterized by lower-symmetry and much larger EFGs, the most likely sites retain the trigonal rotation axis [e.g., 6*c* at (0, 0, 1/3)]. A simple point-charge model of isolated $^8Li^+$ in the BTS lattice, using ionic charges of +0.3 for Bi and -0.2 for Se/Te ($\frac{1}{10}$ their nominal values), gives $\nu_q$ for these sites that are within a factor ∼3 of the values for the 3*b* site in the vdW gap (∼2 kHz), consistent with the difference required to explain the experimental spectra. Note that, while the point-charge model predicts nearly identical $|\nu_q|$ for all sites in the vdW gap, sites on the edges of the hexagons in Fig. 12 have the *opposite* sign.

From the helicity-resolved resonances, the sign of the EFG does not change with temperature and, based on the *T* independent $\nu_q$ and satellite amplitudes, we suggest that this component corresponds to a fraction of implanted $^8Li^+$ that stops at a site within the QL, where it remains static over its lifetime. Similarly, we ascribe the unsplit line to $^8Li^+$ stopped in the vdW gap, likely in the 3*b* site. This component, in contrast, is dynamic above 100 K, accounting for the growth in resonance amplitude and the $1/T_1$ maxima, which we consider in more detail in Sec. IV A. Note that we find no evidence for a site change transition up to 317 K, indicating a substantial energy barrier separates the two sites.


[1] R. J. Cava, H. Ji, M. K. Fuccillo, Q. D. Gibson, and Y. S. Hor, Crystal structure and chemistry of topological insulators, J. Mater. Chem. C **1**, 3176 (2013).

[2] J. P. Heremans, R. J. Cava, and N. Samarth, Tetradymites as thermoelectrics and topological insulators, Nat. Rev. Mater. **2**, 17049 (2017).

[3] M. Z. Hasan and C. L. Kane, *Colloquium*: Topological insulators, Rev. Mod. Phys. **82**, 3045 (2010).

[4] M. Z. Hasan and J. E. Moore, Three-dimensional topological insulators, Annu. Rev. Condens. Matter Phys. **2**, 55 (2011).

[5] Y. S. Hor, A. Richardella, P. Roushan, Y. Xia, J. G. Checkelsky, A. Yazdani, M. Z. Hasan, N. P. Ong, and R. J. Cava, *p*-type $Bi_2Se_3$ for topological insulator and low-temperature thermoelectric applications, Phys. Rev. B **79**, 195208 (2009).

[6] D. Hsieh, Y. Xia, D. Qian, L. Wray, J. H. Dil, F. Meier, J. Osterwalder, L. Patthey, J. G. Checkelsky, N. P. Ong, A. V. Fedorov, H. Lin, A. Bansil, D. Grauer, Y. S. Hor, R. J. Cava, and M. Z. Hasan, A tunable topological insulator in the spin helical dirac transport regime, Nature (London) **460**, 1101 (2009).

[7] S. Nakajima, The crystal structure of $Bi_2Te_{3-x}Se_x$, J. Phys. Chem. Solids **24**, 479 (1963).

[8] S. Jia, H. Ji, E. Climent-Pascual, M. K. Fuccillo, M. E. Charles, J. Xiong, N. P. Ong, and R. J. Cava, Low-carrier-concentration crystals of the topological insulator $Bi_2Te_2Se$, Phys. Rev. B **84**, 235206 (2011).

[9] D. O. Scanlon, P. D. C. King, R. P. Singh, A. de la Torre, S. McKeown Walker, G. Balakrishnan, F. Baumberger, and C. R. A. Catlow, Controlling bulk conductivity in topological insulators: Key role of anti-site defects, Adv. Mater. **24**, 2154 (2012).

[10] A. Akrap, M. Tran, A. Ubaldini, J. Teyssier, E. Giannini, D. van der Marel, P. Lerch, and C. C. Homes, Optical properties of $Bi_2Te_2Se$ at ambient and high pressures, Phys. Rev. B **86**, 235207 (2012).

[11] Z. Ren, A. A. Taskin, S. Sasaki, K. Segawa, and Y. Ando, Large bulk resistivity and surface quantum oscillations in the topological insulator $Bi_2Te_2Se$, Phys. Rev. B **82**, 241306 (2010).

[12] J. Xiong, A. C. Petersen, D. Qu, Y. S. Hor, R. J. Cava, and N. P. Ong, Quantum oscillations in a topological insulator $Bi_2Te_2Se$ with large bulk resistivity (6 Ω cm), Physica E (Amsterdam) **44**, 917 (2012).

[13] J. Xiong, Y. Luo, Y. H. Khoo, S. Jia, R. J. Cava, N. P. Ong, High-field Shubnikov-de Haas oscillations in the topological insulator $Bi_2Te_2Se$, Phys. Rev. B **86**, 045314 (2012).

[14] M. Neupane, S.-Y. Xu, L. A. Wray, A. Petersen, R. Shankar, N. Alidoust, C. Liu, A. Fedorov, H. Ji, J. M. Allred, Y. S. Hor, T.-R. Chang, H.-T. Jeng, H. Lin, A. Bansil, R. J. Cava, and M. Z. Hasan, Topological surface states and Dirac point tuning in ternary topological insulators, Phys. Rev. B **85**, 235406 (2012).

[15] K. Miyamoto, A. Kimura, T. Okuda, H. Miyahara, K. Kuroda, H. Namatame, M. Taniguchi, S. V. Eremeev, T. V. Menshchikova, E. V. Chulkov, K. A. Kokh, and O. E. Tereshchenko, Topological Surface States with Persistent High Spin Polarization Across the Dirac Point in $Bi_2Te_2Se$ and $Bi_2Se_2Te$, Phys. Rev. Lett. **109**, 166802 (2012).

[16] M. Nurmamat, E. E. Krasovskii, K. Kuroda, M. Ye, K. Miyamoto, M. Nakatake, T. Okuda, H. Namatame, M. Taniguchi, E. V. Chulkov, K. A. Kokh, O. E. Tereshchenko, and A. Kimura, Unoccupied topological surface state in $Bi_2Te_2Se$, Phys. Rev. B **88**, 081301 (2013).

[17] M. Neupane, S.-Y. Xu, Y. Ishida, S. Jia, B. M. Fregoso, C. Liu, I. Belopolski, G. Bian, N. Alidoust, T. Durakiewicz, V. Galitski, S. Shin, R. J. Cava, and M. Z. Hasan, Gigantic Surface Lifetime of An Intrinsic Topological Insulator, Phys. Rev. Lett. **115**, 116801 (2015).

[18] E. Frantzeskakis, S. V. Ramankutty, N. de Jong, Y. K. Huang, Y. Pan, A. Tytarenko, M. Radovic, N. C. Plumb, M. Shi, A. Varykhalov, A. de Visser, E. van Heumen, and M. S. Golden, Trigger of the Ubiquitous Surface Band Bending in 3D Topological Insulators, Phys. Rev. X **7**, 041041 (2017).

[19] M. Nurmamat, E. E. Krasovskii, Y. Ishida, K. Sumida, J. Chen, T. Yoshikawa, E. V. Chulkov, K. A. Kokh, O. E. Tereshchenko, S. Shin, and A. Kimura, Ultrafast dynamics of an unoccupied surface resonance state in $Bi_2Te_2Se$, Phys. Rev. B **97**, 115303 (2018).

[20] K. Momma and F. Izumi, VESTA 3 for three-dimensional visualization of crystal, volumetric and morphology data, J. Appl. Crystallogr. **44**, 1272 (2011).

[21] J. Korringa, Nuclear magnetic relaxation and resonnance line shift in metals, Physica (Amsterdam) **16**, 601 (1950).

[22] C. P. Slichter, *Principles of Magnetic Resonance*, 3rd ed., Springer Series in Solid-State Sciences, Vol. 1 (Springer, Berlin, 1990).

[23] M. M. Vazifeh and M. Franz, Spin response of electrons on the surface of a topological insulator, Phys. Rev. B **86**, 045451 (2012).

[24] D. M. Nisson, A. P. Dioguardi, P. Klavins, C. H. Lin, K. Shirer, A. C. Shockley, J. Crocker, and N. J. Curro, Nuclear magnetic resonance as a probe of electronic states of $Bi_2Se_3$, Phys. Rev. B **87**, 195202 (2013).

[25] S. Mukhopadhyay, S. Krämer, H. Mayaffre, H. F. Legg, M. Orlita, C. Berthier, M. Horvatić, G. Martinez, M. Potemski, B. A. Piot, A. Materna, G. Strzelecka, and A. Hruban, Hyperfine coupling and spin polarization in the bulk of the topological insulator $Bi_2Se_3$, Phys. Rev. B **91**, 081105 (2015).

[26] B.-L. Young, Z.-Y. Lai, Z. Xu, A. Yang, G. D. Gu, Z.-H. Pan, T. Valla, G. J. Shu, R. Sankar, and F. C. Chou, Probing the bulk electronic states of $Bi_2Se_3$ using nuclear magnetic resonance, Phys. Rev. B **86**, 075137 (2012).

[27] D. Koumoulis, B. Leung, T. C. Chasapis, R. Taylor, D. King, M. G. Kanatzidis, and L.-S. Bouchard, Understanding bulk defects in topological insulators from nuclear-spin interactions, Adv. Funct. Mater. **24**, 1519 (2014).

[28] D. Koumoulis, T. C. Chasapis, R. E. Taylor, M. P. Lake, D. King, N. N. Jarenwattananon, G. A. Fiete, M. G. Kanatzidis, and L.-S. Bouchard, NMR Probe of Metallic States in Nanoscale Topological Insulators, Phys. Rev. Lett. **110**, 026602 (2013).

[29] M. Bianchi, D. Guan, S. Bao, J. Mi, B. B. Iversen, P. D. C. King, and P. Hofmann, Coexistence of the topological state and a two-dimensional electron gas on the surface of $Bi_2Se_3$, Nat. Commun. **1**, 128 (2010).

[30] D. Yu. Podorozhkin, E. V. Charnaya, A. Antonenko, R. Mukhamad'yarov, V. V. Marchenkov, S. V. Naumov, J. C. A. Huang, H. W. Weber, and A. S. Bugaev, Nuclear magnetic resonance study of a $Bi_2Te_3$ topological insulator, Phys. Solid State **57**, 1741 (2015).

[31] N. M. Georgieva, D. Rybicki, R. Guehne, G. V. M. Williams, S. V. Chong, K. Kadowaki, I. Garate, and J. Haase, $^{77}$Se nuclear magnetic resonance of topological insulator $Bi_2Se_3$, Phys. Rev. B **93**, 195120 (2016).

[32] A. O. Antonenko, E. V. Charnaya, D. Yu. Nefedov, D. Yu. Podorozhkin, A. V. Uskov, A. S. Bugaev, M. K. Lee, L. J. Chang, S. V. Naumov, Yu. A. Perevozchikova, V. V. Chistyakov, J. C. A. Huang, and V. V. Marchenkov, NMR study of topological insulator $Bi_2Te_3$ in a wide temperature range, Phys. Solid State **59**, 2331 (2017).

[33] W. A. MacFarlane, Implanted-ion $\beta$NMR: A new probe for nanoscience, Solid State Nucl. Magn. Reson. **68–69**, 1 (2015).

[34] P. Bakule and E. Morenzoni, Generation and applications of slow polarized muons, Contemp. Phys. **45**, 203 (2004).

[35] H. Ackermann, P. Heitjans, and H.-J. Stöckmann, $\beta$ emitters and isomeric nuclei as probes in condensed matter, in *Hyperfine Interactions of Radioactive Nuclei*, Topics in Current Physics, Vol. 31, edited by Jens Christiansen (Springer, Berlin, 1983), Chap. 6, pp. 291–361.

[36] M. H. Cohen and F. Reif, Quadrupole effects in nuclear magnetic resonance studies of solids, in *Solid State Physics*, Vol. 5, edited by Frederick Seitz and David Turnbull (Academic, New York, 1957), pp. 321–438.

[37] N. Bloembergen, E. M. Purcell, and R. V. Pound, Relaxation effects in nuclear magnetic resonance absorption, Phys. Rev. **73**, 679 (1948).

[38] P. M. Richards, Magnetic resonance in superionic conductors, in *Physics of Superionic Conductors*, Topics in Current Physics, Vol. 15, edited by Myron B. Salamon (Springer, Berlin, 1979), Chap. 6, pp. 141–174.

[39] P. A. Beckmann, Spectral densities and nuclear spin relaxation in solids, Phys. Rep. **171**, 85 (1988).

[40] S. F. J. Cox, Muonium as a model for interstitial hydrogen in the semiconducting and semimetallic elements, Rep. Prog. Phys. **72**, 116501 (2009).

[41] J. A. Krieger, C.-Z. Chang, M.-A. Husanu, D. Sostina, A. Ernst, M. M. Otrokov, T. Prokscha, T. Schmitt, A. Suter, M. G. Vergniory, E. V. Chulkov, J. S. Moodera, V. N. Strocov, and Z. Salman, Spectroscopic perspective on the interplay between electronic and magnetic properties of magnetically doped topological insulators, Phys. Rev. B **96**, 184402 (2017).

[42] L. B. Duffy, N.-J. Steinke, J. A. Krieger, A. I. Figueroa, K. Kummer, T. Lancaster, S. R. Giblin, F. L. Pratt, S. J. Blundell, T. Prokscha, A. Suter, S. Langridge, V. N. Strocov, Z. Salman, G. van der Laan, and T. Hesjedal, Microscopic effects of Dy doping in the topological insulator $Bi_2Te_3$, Phys. Rev. B **97**, 174427 (2018).

[43] H. Leng, D. Cherian, Y. K. Huang, J.-C. Orain, A. Amato, and A. de Visser, Muon spin rotation study of the topological superconductor $Sr_xBi_2Se_3$, Phys. Rev. B **97**, 054503 (2018).

[44] J. A. Krieger, A. Kanigel, A. Ribak, E. Pomjakushina, K. B. Chashka, K. Conder, E. Morenzoni, T. Prokscha, A. Suter, and Z. Salman, Superconducting properties of Cu intercalated $Bi_2Se_3$ studied by muon spin spectroscopy, JPS Conf. Proc. **21**, 011028 (2018).

[45] G. D. Morris, W. A. MacFarlane, K. H. Chow, Z. Salman, D. J. Arseneau, S. Daviel, A. Hatakeyama, S. R. Kreitzman, C. D. P. Levy, R. Poutissou, R. H. Heffner, J. E. Elenewski, L. H. Greene, and R. H. Kiefl, Depth-Controlled $\beta$-NMR of $^8$Li in a Thin Silver Film, Phys. Rev. Lett. **93**, 157601 (2004).

[46] Z. Salman, E. P. Reynard, W. A. MacFarlane, K. H. Chow, J. Chakhalian, S. R. Kreitzman, S. Daviel, C. D. P. Levy, R. Poutissou, and R. F. Kiefl, $\beta$-detected nuclear quadrupole resonance with a low-energy beam of $^8Li^+$, Phys. Rev. B **70**, 104404 (2004).

[47] G. D. Morris, $\beta$-NMR, Hyperfine Int. **225**, 173 (2014).

[48] W. A. MacFarlane, C. D. P. Levy, M. R. Pearson, T. Buck, K. H. Chow, A. N. Hariwal, R. F. Kiefl, F. H. McGee, G. D. Morris, and D. Wang, The initial state of optically polarized $^8Li^+$ from the $\beta$-NMR in bismuth, J. Phys.: Conf. Ser. **551**, 012059 (2014).

[49] Z. Salman, R. F. Kiefl, K. H. Chow, M. D. Hossain, T. A. Keeler, S. R. Kreitzman, C. D. P. Levy, R. I. Miller, T. J. Parolin, M. R. Pearson, H. Saadaoui, J. D. Schultz, M. Smadella, D. Wang, and W. A. MacFarlane, Near-Surface Structural Phase Transition of $SrTiO_3$ Studied with Zero-field $\beta$-Detected Nuclear Spin Relaxation and Resonance, Phys. Rev. Lett. **96**, 147601 (2006).

[50] W. A. MacFarlane, Q. Song, N. J. C. Ingle, K. H. Chow, M. Egilmez, I. Fan, M. D. Hossain, R. F. Kiefl, C. D. P. Levy, G. D. Morris, T. J. Parolin, M. R. Pearson, H. Saadaoui, Z. Salman, and D. Wang, $\beta$-detected NMR spin relaxation in a thin film heterostructure of ferromagnetic EuO, Phys. Rev. B **92**, 064409 (2015).

[51] W. A. MacFarlane, T. J. Parolin, D. L. Cortie, K. H. Chow, M. D. Hossain, R. F. Kiefl, C. D. P. Levy, R. M. L. McFadden, G. D. Morris, M. R. Pearson, H. Saadaoui, Z. Salman, Q. Song, and D. Wang, $^8Li^+\beta$-NMR in the cubic insulator MgO, J. Phys.: Conf. Ser. **551**, 012033 (2014).

[52] M. D. Hossain, H. Saadaoui, T. J. Parolin, Q. Song, D. Wang, M. Smadella, K. H. Chow, M. Egilmez, I. Fan, R. F. Kiefl, S. R. Kreitzman, C. D. P. Levy, G. D. Morris, M. R. Pearson, Z. Salman, and W. A. MacFarlane, The spin lattice relaxation of $^8$Li in simple metals, Physica B (Amsterdam) **404**, 914 (2009).

[53] W. A. MacFarlane, C. B. L. Tschense, T. Buck, K. H. Chow, D. L. Cortie, A. N. Hariwal, R. F. Kiefl, D. Koumoulis, C. D. P. Levy, I. McKenzie, F. H. McGee, G. D. Morris, M. R. Pearson, Q. Song, D. Wang, Y. S. Hor, and R. J. Cava, $\beta$-detected NMR of $^8Li^+$ in Bi, Sb, and the topological insulator $Bi_{0.9}Sb_{0.1}$, Phys. Rev. B **90**, 214422 (2014).

[54] D. Wang, M. D. Hossain, Z. Salman, D. Arseneau, K. H. Chow, S. Daviel, T. A. Keeler, R. F. Kiefl, S. R. Kreitzman, C. D. P. Levy, G. D. Morris, R. I. Miller, W. A. MacFarlane, T. J. Parolin, and H. Saadaoui, $\beta$-detected NMR of $^8$Li in the normal state of $2H$-$NbSe_2$, Physica B (Amsterdam) **374–375**, 239 (2006).

[55] M. D. Hossain, Z. Salman, D. Wang, K. H. Chow, S. Kreitzman, T. A. Keeler, C. D. P. Levy, W. A. MacFarlane, R. I. Miller, G. D. Morris, T. J. Parolin, M. Pearson, H. Saadaoui, and R. F. Kiefl, Low-field cross spin relaxation of $^8$Li in superconducting $NbSe_2$, Phys. Rev. B **79**, 144518 (2009).

[56] W. A. MacFarlane, K. H. Chow, M. D. Hossain, V. L. Karner, R. F. Kiefl, R. M. L. McFadden, G. D. Morris, H. Saadaoui, and Z. Salman, The spin relaxation of $^8Li^+$ in gold at low magnetic field, JPS Conf. Proc. **21**, 011020 (2018).

[57] W. A. MacFarlane, J. Bobroff, H. Alloul, P. Mendels, N. Blanchard, G. Collin, and J.-F. Marucco, Dynamics of the Local Moment Induced by Nonmagnetic Defects in Cuprates, Phys. Rev. Lett. **85**, 1108 (2000).

[58] K. D. Becker, Nuclear magnetic relaxation induced by the dynamics of lattice defects in solids ($I = 3/2$, $I = 2$, and $I = 5/2$), Z. Naturforsch. A **37**, 697 (1982).

[59] E. M. Levin, T. M. Riedemann, A. Howard, N. H. Jo, S. L. Bud'ko, P. C. Canfield, and T. A. Lograsso, $^{125}$Te NMR and seebeck effect in $Bi_2Te_3$ synthesized from stoichiometric and Te-rich melts, J. Phys. Chem. C **120**, 25196 (2016).

[60] F. James and M. Roos, MINUIT–a system for function minimization and analysis of the parameter errors and correlations, Comput. Phys. Commun. **10**, 343 (1975).

[61] R. Brun and F. Rademakers, ROOT–an object oriented data analysis framework, Nucl. Instrum. Methods Phys. Res., Sect. A **389**, 81 (1997).

[62] C. A. Sholl, Nuclear spin relaxation by translational diffusion in liquids and solids: high- and low-frequency limits, J. Phys. C: Solid State Phys. **14**, 447 (1981).

[63] A. Yelon, B. Movaghar, and R. S. Crandall, Multi-excitation entropy: its role in thermodynamics and kinetics, Rep. Prog. Phys. **69**, 1145 (2006).

[64] Z.-Z. Gan and P. A. Lee, Nuclear-spin relaxation near the metal-insulator transition, Phys. Rev. B **33**, 3595 (1986).

[65] K. Paraskevopoulos, E. Hatzikraniotis, K. Chrisafis, M. Zamani, J. Stoemenos, N. A. Economou, K. Alexiadis, and M. Balkanski, Intercalation studies in bismuth selenide, Mater. Sci. Eng., B **1**, 147 (1988).

[66] J. Bludská, I. Jakubec, S. Karamazov, J. Horák, and C. Uher, Lithium ions in the van der waals gap of $Bi_2Se_3$ single crystals, J. Solid State Chem. **183**, 2813 (2010).

[67] W. Küchler, P. Heitjans, A. Payer, and R. Schöllhorn, $^7$Li NMR relaxation by diffusion in hexagonal and cubic $Li_xTiS_2$, Solid State Ionics **70–71**, 434 (1994).

[68] R. M. L. McFadden, T. J. Buck, A. Chatzichristos, C.-C. Chen, K. H. Chow, D. L. Cortie, M. H. Dehn, V. L. Karner, D. Koumoulis, C. D. P. Levy, C. Li, I. McKenzie, R. Merkle, G. D. Morris, M. R. Pearson, Z. Salman, D. Samuelis, M. Stachura, J. Xiao, J. Maier, R. F. Kiefl, and W. A. MacFarlane, Microscopic dynamics of $Li^+$ in rutile $TiO_2$ revealed by $^8$Li $\beta$-detected nuclear magnetic resonance, Chem. Mater. **29**, 10187 (2017).

[69] H. Saadaoui, G. D. Morris, Z. Salman, Q. Song, K. H. Chow, M. D. Hossain, C. D. P. Levy, T. J. Parolin, M. R. Pearson, M. Smadella, D. Wang, L. H. Greene, P. J. Hentges, R. F. Kiefl, and W. A. MacFarlane, Search for broken time-reversal symmetry near the surface of superconducting $YBa_2Cu_3O_{7-\delta}$ films using $\beta$-detected nuclear magnetic resonance, Phys. Rev. B **83**, 054504 (2011).

[70] R. O. Carlson, Anisotropic diffusion of copper into bismuth telluride, J. Phys. Chem. Solids **13**, 65 (1960).

[71] J. D. Keys and H. M. Dutton, Diffusion and solid solubility of silver in single-crystal bismuth telluride, J. Phys. Chem. Solids **24**, 563 (1963).

[72] J. T. Folinsbee, A. M. Simpson, and M. H. Jericho, Li diffusion in $NbSe_2$ and $Ag_{0.25}NbSe_2$ single crystals, Mater. Res. Bull. **21**, 961 (1986).

[73] J. B. Maclachlan, W. H. Kruesi, and D. J. Fray, Intercalation of copper into bismuth telluride, J. Mater. Sci. **27**, 4223 (1992).

[74] M. Wilkening, W. Küchler, and P. Heitjans, From Ultraslow to Fast Lithium Diffusion in the 2D Ion Conductor $Li_{0.7}TiS_2$ Probed Directly by Stimulated-Echo NMR and Nuclear Magnetic Relaxation, Phys. Rev. Lett. **97**, 065901 (2006).

[75] M. Wilkening and P. Heitjans, Li jump process in $h$-$Li_{0.7}TiS_2$ studied by two-time $^7$Li spin-alignment echo NMR and comparison with results on two-dimensional diffusion from nuclear magnetic relaxation, Phys. Rev. B **77**, 024311 (2008).

[76] M. A. Gosálvez, M. M. Otrokov, N. Ferrando, A. G. Ryabishchenkova, A. Ayuela, P. M. Echenique, and E. V. Chulkov, Low-coverage surface diffusion in complex periodic energy landscapes. II. Analytical solution for systems with asymmetric hops, Phys. Rev. B **93**, 205416 (2016).

[77] H. Selbach, O. Kanert, and D. Wolf, NMR investigation of the diffusion and conduction properties of the semiconductor tellurium. I. Electronic properties, Phys. Rev. B **19**, 4435 (1979).

[78] F. Bridges and W. G. Clark, Quantum and other oscillations of the nuclear spin-lattice relaxation rate in $n$-InSb, Phys. Rev. **182**, 463 (1969).

[79] S. Jia, H. Beidenkopf, I. Drozdov, M. K. Fuccillo, J. Seo, J. Xiong, N. P. Ong, A. Yazdani, and R. J. Cava, Defects and high bulk resistivities in the Bi-rich tetradymite topological insulator $Bi_{2+x}Te_{2-x}Se$, Phys. Rev. B **86**, 165119 (2012).

[80] A. Hashibon and C. Elsässer, First-principles density functional theory study of native point defects in $Bi_2Te_3$, Phys. Rev. B **84**, 144117 (2011).

[81] M. Brahlek, N. Koirala, N. Bansal, and S. Oh, Transport properties of topological insulators: Band bending, bulk metal-to-insulator transition, and weak anti-localization, Solid State Commun. **215–216**, 54 (2015).

[82] Z. Salman, A. I. Mansour, K. H. Chow, M. Beaudoin, I. Fan, J. Jung, T. A. Keeler, R. F. Kiefl, C. D. P. Levy, R. C. Ma, G. D. Morris, T. J. Parolin, D. Wang, and W. A. MacFarlane, $\beta$-NMR of isolated $^8Li^+$ implanted into a thin copper film, Phys. Rev. B **75**, 073405 (2007).

[83] T. J. Parolin, Z. Salman, K. H. Chow, Q. Song, J. Valiani, H. Saadaoui, A. O'Halloran, M. D. Hossain, T. A. Keeler, R. F. Kiefl, S. R. Kreitzman, C. D. P. Levy, R. I. Miller, G. D. Morris, M. R. Pearson, M. Smadella, D. Wang, M. Xu, and W. A. MacFarlane, High resolution $\beta$-NMR study of $^8Li^+$ implanted in gold, Phys. Rev. B **77**, 214107 (2008).

[84] D. Wang, Z. Salman, K. H. Chow, I. Fan, M. D. Hossain, T. A. Keeler, R. F. Kiefl, C. D. P. Levy, A. I. Mansour, G. D. Morris, M. R. Pearson, T. J. Parolin, H. Saadaoui, M. Smadella, Q. Song, and W. A. MacFarlane, Nuclear spin relaxation/resonance of $^8$Li in Al, Physica B (Amsterdam) **404**, 920 (2009).

[85] O. Ofer, K. H. Chow, I. Fan, M. Egilmez, T. J. Parolin, M. D. Hossain, J. Jung, Z. Salman, R. F. Kiefl, C. D. P. Levy, G. D. Morris, M. R. Pearson, H. Saadaoui, Q. Song, D. Wang, and W. A. MacFarlane, $\beta$-NMR study of isolated $^8Li^+$ in the enhanced paramagnet platinum, Phys. Rev. B **86**, 064419 (2012).

[86] C. H. Pennington and V. A. Stenger, Nuclear magnetic resonance of $C_{60}$ and fulleride superconductors, Rev. Mod. Phys. **68**, 855 (1996).

[87] W. W. Warren, Nuclear magnetic resonance and relaxation in the "liquid semiconductors" $In_2Te3$, $Ga_2Te_3$, and $Sb_2Te_3$, Phys. Rev. B **3**, 3708 (1971).

[88] W. Götze and W. Ketterle, Nuclear spin relaxation in disordered conductors, Z. Phys. B: Condens. Matter **54**, 49 (1983).

[89] B. S. Shastry and E. Abrahams, What Does the Korringa Ratio Measure? Phys. Rev. Lett. **72**, 1933 (1994).

[90] M. J. R. Hoch and D. F. Holcomb, $^{31}$P Knight shifts and spin dynamics in Si:P at temperatures comparable to the fermi temperature, Phys. Rev. B **71**, 035115 (2005).

[91] E. M. Meintjes, J. Danielson, and W. W. Warren, Temperature-dependent NMR study of the impurity state in heavily doped Si:P, Phys. Rev. B **71**, 035114 (2005).

[92] M. A. Paalanen, A. E. Ruckenstein, and G. A. Thomas, Spins in Si:P Close to the Metal-Insulator Transition, Phys. Rev. Lett. **54**, 1295 (1985).

[93] H. Alloul and P. Dellouve, Spin Localization in Si:P—Direct Evidence from $^{31}$P NMR, Phys. Rev. Lett. **59**, 578 (1987).

[94] Y. Yafet, R. W. Keyes, and E. N. Adams, Hydrogen atom in a strong magnetic field, J. Phys. Chem. Solids **1**, 137 (1956).

[95] M. I. Dyakonov, A. L. Efros, and D. L. Mitchell, Magnetic freeze-out of electrons in extrinsic semiconductors, Phys. Rev. **180**, 813 (1969).

[96] B. A. Assaf, T. Cardinal, P. Wei, F. Katmis, J. S. Moodera, and D. Heiman, Linear magnetoresistance in topological insulator thin films: Quantum phase coherence effects at high temperatures, Appl. Phys. Lett. **102**, 012102 (2013).

[97] J. Xiong, Y. Khoo, S. Jia, R. J. Cava, and N. P. Ong, Tuning the quantum oscillations of surface Dirac electrons in the topological insulator $Bi_2Te_2Se$ by liquid gating, Phys. Rev. B **88**, 035128 (2013).

[98] B. M. Fregoso and S. Coh, Intrinsic surface dipole in topological insulators, J. Phys.: Condens. Matter **27**, 422001 (2015).

[99] H. Maebashi, T. Hirosawa, M. Ogata, and H. Fukuyama, Nuclear magnetic relaxation and Knight shift due to orbital interaction in Dirac electron systems, J. Phys. Chem. Solids, doi:10.1016/j.jpcs.2017.12.034.

[100] S. Kolkowitz, A. Safira, A. A. High, R. C. Devlin, S. Choi, Q. P. Unterreithmeier, D. Patterson, A. S. Zibrov, V. E. Manucharyan, H. Park, and M. D. Lukin, Probing Johnson noise and ballistic transport in normal metals with a single-spin qubit, Science **347**, 1129 (2015).

[101] P. Lee and N. Nagaosa, Relaxation of nuclear spin due to long-range orbital currents, Phys. Rev. B **43**, 1223 (1991).

[102] A. Knigavko, B. Mitrović, and K. V. Samokhin, Divergence of the orbital nuclear magnetic relaxation rate in metals, Phys. Rev. B **75**, 134506 (2007).

[103] T. Hirosawa, H. Maebashi, and M. Ogata, Nuclear spin relaxation time due to the orbital currents in Dirac electron systems, J. Phys. Soc. Jpn. **86**, 063705 (2017).

[104] T. Bömerich, J. Lux, Q. T. Feng, and A. Rosch, Length scale of puddle formation in compensation-doped semiconductors and topological insulators, Phys. Rev. B **96**, 075204 (2017).

[105] R. E. Taylor, B. Leung, M. P. Lake, and L.-S. Bouchard, Spin-lattice relaxation in bismuth chalcogenides, J. Phys. Chem. C **116**, 17300 (2012).

[106] J. F. Ziegler, J. P. Biersack, and M. D. Ziegler, *SRIM: The Stopping and Range of Ions in Matter*, 7th ed. (SRIM Co., 2008), http://www.srim.org/.

[107] *Crystallography and Crystal Chemistry of Materials with Layered Structures*, Physics and Chemistry of Materials with Layered Structures, Vol. 2, edited by F. Lévy (Springer, Dordrecht, 1976).

[108] H. P. Dibbs and J. R. Tremblay, Thermal diffusion of silver in single-crystal bismuth telluride, J. Appl. Phys. **39**, 2976 (1968).

[109] M. C. Shaughnessy, N. C. Bartelt, J. A. Zimmerman, and J. D. Sugar, Energetics and diffusion of gold in bismuth telluride-based thermoelectric compounds, J. Appl. Phys. **115**, 063705 (2014).

[110] A. A. Kuliev and G. B. Abdullaev, An investigation of the diffusion of Zn and Se in $Bi_2Se_3$, BiSe and CdSb, Fiz. Tverd. Tela **1**, 603 (1959) [Sov. Phys. - Solid State **1**, 545 (1959)].

[111] Z. Ding, S. K. Bux, D. J. King, F. L. Chang, T.-H. Chen, S.-C. Huang, and R. B. Kaner, Lithium intercalation and exfoliation of layered bismuth selenide and bismuth telluride, J. Mater. Chem. **19**, 2588 (2009).

[112] J. Chen, Y. Zhu, N. Chen, X. Liu, Z. Sun, Z. Huang, F. Kang, Q. Gao, J. Jiang, and L. Chen, Nano-scaled top-down of bismuth chalcogenides based on electrochemical lithium intercalation, J. Nanopart. Res. **13**, 6569 (2011).